"Dynamic Loading of Polycrystalline Shape Memory Alloy Rods," by D.C. Lagoudas, K. ravi-Chandar, K. Sarh and P. Popov, Submitted 5/28/02, MoM

Dynamic Loading of Polycrystalline Shape Memory Alloy Rods

Dimitris C. Lagoudas [a,*], K. Ravi-Chandar [b], Khalid Sarh [c],
Peter Popov [a]

[a] *Department Of Aerospace Engineering,*
Texas A&M University, TX 77843-3141, USA

[b] *Department of Aerospace Engineering and Engineering Mechanics,*
University of Texas at Austin, Austin, TX 78712-1085, USA

[c] *Department of Mechanical Engineering,*
University of Houston, TX 77204-4792, USA

DISTRIBUTION STATEMENT A
Approved for Public Release
Distribution Unlimited

20020715 105

Abstract

Shape Memory Alloys (SMAs) have recently been considered for dynamic loading applications for energy absorbing and vibration damping devices. An SMA body subjected to external dynamic loading will experience large inelastic deformations that will propagate through the body as phase transformation and/or detwinning shock waves. The wave propagation problem in a cylindrical polycrystalline SMA rod induced by an impact loading is considered in this paper. Numerical solutions for various boundary conditions are presented for stress induced martensite and detwinning of martensite. The numerical simulations utilize an adaptive Finite Element Method (FEM) based on the Zienkiewicz-Zhu (ZZ) error estimator. Selected results are compared to known analytical solutions to verify the adaptive FEM approach. The energy dissipation in an SMA rod is evaluated for a square pulse stress input applied at various temperatures involving both stress induced martensite and detwinning of martensite. The dynamic response of a NiTi SMA rod is also studied experimentally in a split Hopkinson bar apparatus under detwinning conditions. Strain history records obtained by strain gauges placed at different locations along the SMA rod are compared with numerical simulations for a square pulse stress input. The quasi-static and dynamic stress-strain hysteretic response of the SMA, both due to detwinning, are found to be nearly identical. The quasi-static tests are used to calibrate the rate independent constitutive model used for the numerical simulations, which are found to match the experimental observations reasonably well.

Key words: Shape Memory Alloy, Dynamic Analysis, Adaptive FEM, Hopkinson Bar

---

Preprint submitted to Mechanics of Materials *27 May 2002*

1 Introduction

There are many areas of applications which can successfully utilize the unique properties of SMAs. The engineering research presented in this paper relates directly to the design of SMA components capable of absorbing dynamic loads. Such components can be integrated into critical parts of structures that may need protection from impact loads. Examples include joints that connect the hull of an underwater vehicle with its internal structure, tank armor or blast resistant cargo containers. Another promising field of application includes various active or passive vibration damping devices. Many different SMA devices have been proposed among which nonlinear hysteretic SMA springs (Yiu and Regelbrugge, 1995; Graesser, 1995), wires (Thomson et al., 1995; Fosdick and Ketema, 1998) or rods (Feng and Li, 1996). In a recent paper (Lagoudas et al., 2001) the authors investigate numerically the vibration damping capabilities of SMAs.

Shape Memory Alloys are a class of materials that change their internal structure due to changes in temperature and/or externally applied loads. At high temperatures the crystal lattice is in the high symmetry austenite phase (A). At low temperatures the material exists in a low symmetry martensite phase (M). The austenite to martensite phase transition is diffusionless and is characterized by shear deformations of entire regions inside the material (Wayman, 1983). What makes SMA materials remarkably different from ordinary metals is the *shape memory effect* and the effect of *pseudoelasticity* which are associated with the specific way the phase transition occurs (Funakubo, 1987). The *shape memory effect* allows material which has been deformed while in the martensitic phase to recover its shape upon heating. The mechanism behind this behavior is the ability of SMAs to allow detwinning of the self-accomodated martensitic variants. The *pseudelasticity* in SMAs is their ability to support large inelastic strains recoverable upon unloading due to the reverse phase transformation from martensite into austenite. The primary way in which such strains are introduced in the material is the stress induced phase transformation from austenite into martensite. The pseudoelastic response provides both energy dissipation capabilities and shape recovery during the thermomechanical loading path. Utilizing the shape memory effect also leads to dissipation of mechanical energy but the SMA has to be heated after the loading is applied to recover its shape.

Several constitutive models have been developed in recent years to model the shape memory effect and pseudoelasticity of polycrystalline SMAs. Among the

---

* Corresponding author. Tel: 1-979-845-1604; fax: 1-979-845-6051
Email addresses: `lagoudas@aero.tamu.edu` (Dimitris C. Lagoudas), `kravi@mail.utexas.edu` (K. Ravi-Chandar), `ppopov@tamu.edu` (Peter Popov).

most widely accepted rate independent models are the exponential (Tanaka, 1986), cosine (Liang and Rogers, 1990) and polynomial (Boyd and Lagoudas, 1994, 1996). Any of these models can be unified using a thermodynamic framework (Lagoudas et al., 1996) based on the selection of appropriate thermodynamic potentials. This unified constitutive model is extended by Bo and Lagoudas (1999a,b,c,d) to incorporate transformation induced plastic deformations and to account for the evolution of the material behavior during cyclic loading. In the models proposed by Brinson (1993); Brinson and Lammering (1993); Lagoudas and Shu (1999) the martensitic volume fraction is subdivided in two parts to account for thermally induced self-accommodated martensite and stress induced detwinned martensite. A different approach is taken by Abeyaratne et al. (1993, 1994); Abeyaratne and Knowles (1993) who consider a rate dependent constitutive model that allows for softening during phase transformation. Other authors such as Patoor et al. (1996); Siderey et al. (1999); Sun and Hwang (1993a,b) use micromechanical techniques to average the response of the parent austenitic phase and the different martensitic variants to obtain a model for the macroscopic behavior of polycrystalline SMAs. For further details on SMA models the reader is referred to the work by Qidwai and Lagoudas (2000b) as well as the review paper by Birman (1996). In the current work the unified approach (Lagoudas et al., 1996) is chosen over the more complex micromechanical models, assuming rate independence in the constitutive thermomechanical response of SMAs. As it will be shown later such an assumption is confirmed experimentally for the case of detwinning of martensite.

In a recent paper (Chen and Lagoudas, 2000) the rate independent model for polycrystalline SMAs (Lagoudas et al., 1996) is employed to obtain solutions to the coupled thermomechanical problem for SMA materials. The authors take into account the latent heat generation and assuming adiabatic conditions they solve the problem by the method of characteristics together with jump conditions that yield unique solutions. A similar study (Bekker et al., 2002), but for different constitutive models has been carried out for both isothermal and adiabatic conditions. In a different setting Oberaigner et al. (1996) investigates numerically the coupled problem of wave propagation and heat transfer in an SMA rod. The authors focus on stress pulses of low magnitude that cause only elastic deformations. The temperature at one end of the SMA rod is chosen as a function of time in a such a way as to utilize the phase change due to the shape memory effect in order to maximize the damping characteristics of the rod.

The dynamics of phase transformation in piecewise linear elastic materials with non-monotone hysteresis is also studied by Abeyaratne and Knowles (1991). A unique solution is obtained with the use of a kinetic relation controlling the rate of the phase transformation together with a nucleation condition for the initiation of the transformation. In later work the same authors extend the analysis to account for thermal effects (Abeyaratne and Knowles, 1994a,b). In a general setting Pence (1986) considers wave propagating in a nonlinear elastic bar with a non-monotonic stress-strain relationship subjected to a monotonically increasing load. It is found that for sufficiently high loads a strain discontinuity associated with phase transformation is being created.

There has been a limited amount of experimental work done on characterizing the dynamic response of SMAs. An experimental study on the propagation of shear waves in single crystal Cu-Al-Ni shape memory alloy has been done by Escobar and Clifton (1993). Phase transition shocks are not observed directly due to their low propagation speed. Instead, their presence is inferred from the measurements of the elastic waves at the rear end of the specimen. An analytical attempt to model these experiments is presented in Abeyaratne and Knowles (1997). In this work experiments will be conducted on polycrystalline NiTi SMAs.

Classical rate-independent plasticity theory is not sufficient to describe the behavior of SMA materials. While it is still capable of partially predicting the shape memory effect (without capturing the strain recovery upon heating), it cannot model the pseudoelastic response. However, for rate independent models of SMAs both theoretical and experimental developments of dynamic elasto-plasticity can be used for guidance. Theoretical developments on elasto-plastic wave propagation in long rods dates back to the works of Von Karman (1942), Rakhmatulin (1945) and Taylor (1958). Extensive experiments on elasto-plastic wave propagation have been carried out by Bell (1962); Chiddister and Malvern (1963); Kolsky (1949); Clifton and Bodner (1966); Bodner and Clifton (1967) using a split-Hopkinson bar apparatus. The split bar technique itself was introduced by Kolsky (1949). The reader is referred to classical texts on wave propagation such as (Kolsky, 1963; Graff, 1975) for additional information. In recent years there have been extensions to the Hopkinson technique (Nemat-Nasser et al., 1991) that allow for dynamic test recovery in both tension and compression. The basic split-Hopkinson technique will be used in this work to conduct the dynamic experiments on polycrystalline NiTi SMA rods.

The main focus of this paper is the study of the one-dimensional dynamic problem of loading an SMA rod under conditions of pseudoelasticity and detwinning. Both computational and experimental results are obtained. Based on experimental observations the rate independent constitutive model (Lagoudas et al., 1996) is selected. The complex nature of most constitutive models for SMA materials makes direct integration of even the simplest uniaxial transient initial boundary value problems (IBVP) very complicated. Closed form solutions can usually be obtained for simple boundary conditions, e.g. impact step loading (Chen and Lagoudas, 2000) or by simplifying the constitutive model so that the stress can be obtained as an explicit function of strain (Bekker et al., 2002). Numerical solutions of the impact loading problem have been obtained by (Jimenez-Vicktory, 1999; Bekker et al., 2002) by mainly using the Lax-Friedrichs finite difference scheme. This FD scheme has been found to produce a considerable amount of numerical dissipation which makes the distinction between a self-contained nonlinear shock and a rarefaction wave difficult. In this paper numerical simulations of step and pulse shock loading both for stress induced phase transformation and detwinning of martensite are performed using the FEM method. An adaptive meshing technique based on the ZZ error estimator (Zienkiewicz, 1987) is utilized in order to improve the accuracy of the method and decrease computational time. Comparisons with analytical solutions are made whenever such solutions are available. Based on the simulation results, the energy dissipation of SMA rods for pulse loads are discussed.

An experiment on the wave propagation in a SMA rod is also performed in a split-Hopkinson bar apparatus. A nearly equiatomic NiTi SMA specimen instrumented with strain gauges is tested under detwinning conditions for a pulse impact load. Separate tests in a standard uniaxial MTS test frame are performed to establish its quasi-static response. The results of the Hopkinson bar experiment are used to extract the dynamic stress-strain relationship due to detwinning. The adaptive FEM technique is used to simulate the propagation of stress waves in the dynamic experiment.

The paper begins with a brief overview in Section 2 of the field equations and boundary conditions and constitutive model defining the problem. The implementation of the FEM for the NiTi SMA is outlined in Section 3.1. The adaptive strategy is presented in Section 3.2. In order to verify the implementation of the adaptive FEM a boundary value problem with a step-function stress boundary condition is solved in Section 4.1. This specific boundary condition allows for the construction of analytical solutions which can be used to verify the numerical solution methodology. Then, a square pulse IBVP is solved for conditions of stress induced martensite (Section 4.2) and detwinning (Section 4.3). Expected values for energy dissipation as the pulse propagates through the rod are presented. Section 5 describes the split-Hopkinson bar experiment and discusses the dynamic characterization of SMA materials. Finally, in Section 5.4 the numerical schemes developed in this paper are utilized to simulate the experimental results.

2 Field equations and constitutive model for the impact problem of SMA rods

A cylindrical SMA rod of uniform cross-section and length L is considered. A coordinate cover is associated with the centroidal axis of the rod spanning the interval $0 \leq x \leq L$. The rod which is initially stress free and at rest is subjected to an impact load at its left end ($x = 0$). The right end ($x = L$) is assumed to remain traction free. The field equations, initial and boundary conditions are presented next followed by a description of the thermomechanical constitutive model for SMAs.

2.1 Field equations, initial and boundary conditions

The rod is assumed to be long compared to its diameter so it is under uniaxial stress state and the stress $\sigma(x,t)$ depends only on the axial position and time. The axial component of the displacement is denoted by $u(x,t)$. Linearized strain is further assumed so the axial component of the strain $\varepsilon(x,t)$ is related to the displacement by $\varepsilon(x,t) = \partial u / \partial x$. Finally, the density of the material ρ is assumed constant. The local form of the balance of linear momentum and energy then read (Graff, 1975; Malvern, 1977):

$$\rho \frac{\partial^2 u}{\partial t^2} = \frac{\partial \sigma}{\partial x} \tag{1}$$

$$\rho \frac{\partial}{\partial t}\left(\mathcal{U} + \frac{1}{2}\left(\frac{\partial u}{\partial t}\right)^2\right) = \frac{\partial}{\partial x}\left(\frac{\partial u}{\partial t}\sigma - q\right) \tag{2}$$

where $\mathcal{U}$ is the internal energy per unit mass and $q(x,t)$ is the heat flux.

The timescale of the impact problem is on the order of micro- to milliseconds. The physically meaningful IBVP is an adiabatic one because such time-intervals are too short for heat conduction to take place as well as for convection to remove heat through the surface of the rod. In the *adiabatic* approximation, therefore, the heat conduction term q in (2) can be neglected so the balance of energy in conjunction with (1) yields

$$\rho \frac{\partial \mathcal{U}}{\partial t} = \sigma \frac{\partial^2 u}{\partial x \partial t} \tag{3}$$

Equation (1) and (3) involve the field variables u, σ and $\mathcal{U}$. Through appropriate constitutive assumptions to be discussed in the following section only $u(x,t)$ and the temperature $T(x,t)$ will become the independent variables.

For the field variables the following initial and boundary conditions are assumed:

$$u|_{t=0} = 0,\ \frac{\partial u}{\partial t}|_{t=0} = 0,\ T|_{t=0} = T_R \tag{4}$$

$$\sigma|_{x=0} = \sigma_0(t),\ \sigma|_{x=L} = 0 \tag{5}$$

The initial conditions indicate that the rod is at rest and its temperature is equal to the ambient temperature T_R. The boundary conditions specify the traction $\sigma_0(t)$ applied[1] to the left end of the rod. The right end is kept traction free.

2.2 *Thermomechanical constitutive model for polycrystalline SMAs*

The field equations (1), (3) and initial and boundary conditions (4), (5) alone are not sufficient to form a complete IBVP. A thermomechanical constitutive model that captures the key characteristics of pseudoelasticity and detwinning of the SMA response is needed.

2.2.1 *Stress induced martensite*

The constitutive model used is formulated in terms of the Gibbs free energy G and employs the volume fraction of detwinned martensite ξ formed from austenite as an internal variable (Lagoudas et al., 1996). The specific form of G in the one dimensional case is:

$$\begin{aligned} G = G(\sigma, T, \xi) = &-\tfrac{1}{2\rho}\mathcal{S}\sigma^2 - \tfrac{1}{\rho}\sigma\left(\alpha(T - T_R) + \varepsilon^t\right) \\ &+ c\left((T - T_R) - T\ln\left(\tfrac{T}{T_R}\right)\right) - s_0 T + u_0 + f(\xi) \end{aligned} \tag{6}$$

and it is linked to the internal energy $\mathcal{U}$ by a Legendre transformation:

$$\mathcal{U} = G + TS + \tfrac{1}{\rho}\sigma\varepsilon \tag{7}$$

The definition of G includes the inelastic transformation strain ε^t associated with the phase transformation. The function $f(\xi)$ is taken to be a quadratic polynomial in ξ and is responsible for the transformation hardening:

---

[1] There is no continuity requirement on $\sigma_0(t)$ i.e. impact loads are allowed

$$f(\xi) = \begin{cases} \frac{1}{2}\rho b^M \xi^2 + (\mu_1 + \mu_2)\xi, & \dot{\xi} > 0 \\ \frac{1}{2}\rho b^A \xi^2 + (\mu_1 - \mu_2)\xi, & \dot{\xi} < 0 \end{cases} \tag{8}$$

where material constants ρb^A, ρb^M, μ_1 and μ_2 define the transformation surfaces and the hardening during the forward and reverse transitions (Qidwai and Lagoudas, 2000b). In the above $\dot{\xi} > 0$ denotes the forward transformation and $\dot{\xi} < 0$ the reverse. The remaining material properties in (6) are the effective compliance $\mathcal{S}$, effective thermal expansion coefficient α, effective specific heat c, effective specific entropy at the reference state s_0 and effective specific internal energy at the reference state u_0 for the SMAs which is composed of a mixture of austenite and martensite. They are approximated by the following averaging expressions, which are good approximations for polycrystalline SMAs with random orientation distributions for grains (Boyd and Lagoudas, 1994):

$$\begin{aligned} \mathcal{S} = \mathcal{S}(\xi) &= \mathcal{S}^A + \xi \Delta \mathcal{S}, \ \Delta \mathcal{S} := \mathcal{S}^M - \mathcal{S}^A \\ \alpha = \alpha(\xi) &= \alpha^A + \xi \Delta \alpha, \ \Delta \alpha := \alpha^M - \alpha^A \\ c = c(\xi) &= c^A + \xi \Delta c, \ \ \Delta c := c^M - c^A \\ s_0 = s_0(\xi) &= s_0^A + \xi \Delta s_0, \ \Delta s_0 := s_0^M - s_0^A \\ u_0 = u_0(\xi) &= u_0^A + \xi \Delta u_0, \ \Delta u_0 := u_0^M - u_0^A \end{aligned} \tag{9}$$

Quantities with subscript A denote the appropriate material constant for the austenite phase and those with subscript M for the martensite phase. Following a standard thermodynamic procedure the following constitutive relations are obtained:

$$s = -\frac{\partial G}{\partial T} \tag{10}$$

$$\varepsilon = -\rho \frac{\partial G}{\partial \sigma} \tag{11}$$

$$\pi = -\rho \frac{\partial G}{\partial \xi} \tag{12}$$

where s is the entropy and π is the driving force for the transformation. Using (11) the following constitutive relation is obtained:

$$\sigma = E(\xi)(\varepsilon - \alpha(\xi)(T - T_R) - \varepsilon^t) \tag{13}$$

where $E(\xi) = 1/\mathcal{S}(\xi)$ is the effective elastic modulus. The evolution of the inelastic variable ξ is given by a consistency condition derived from a transformation criterion (Lagoudas et al., 1996). The evolution of ε^t follows that of

ξ and in the one dimensional case can be integrated explicitly to yield:

$$\varepsilon^t = Hsgn(\sigma)\xi \tag{14}$$

Here H is a positive material constant corresponding to the maximum transformation strain. The principle of maximum transformation dissipation in conjunction with the second law of thermodynamics leads to the following transformation surface:

$$\pi = \pm Y^* \tag{15}$$

where $Y^* = -\frac{1}{2}\rho\Delta s_0(A^{of} - M^{os}) - \frac{1}{4}\rho\Delta s_0(M^{os} - M^{of} - A^{of} + A^{os})$. The $+Y^*$ at the right hand side stands for the forward ($A \rightarrow M$) transformation surface and $-Y^*$ for the reverse ($M \rightarrow A$) transformation surface. The start and finishing temperature for the forwards transformation are denoted by A^{os} and A^{of} and the start and finishing temperatures for the reverse transformation are denoted by M^{os} and M^{of}, respectively.

For detailed description of the transformation rule and conditions for the forward and reverse phase transformation the reader is referred to the original paper by Lagoudas et al. (1996). The next section describes how detwinning is incorporated into the constitutive model.

2.3 Detwinning of martensite

The detwinning deformation will be accounted for by adapting the constitutive model. The material constants for twinned and detwinned martensite are the same. Consequently, the initial response and the response after the completion of detwinning will both be elastic with the slope being the modulus of elasticity of martensite E^M. The deformation is irreversible upon unloading which, consequently, will also be elastic.

The material constants in the constitutive model can be reinterpreted, replacing the ones for the austenitic phase with the ones for martensite. This will ensure the same elastic response prior the onset of detwinning and after its completion. The internal variable ξ should be interpreted as the volume fraction of detwinned with respect to self-accommodated martensite and H is the maximum inelastic strain. From equation (15) the transformation surface will have the following simple form:

$$\sigma H - \frac{\partial f}{\partial \xi} = 0 \tag{16}$$

The hardening function in this case may be expressed as follows:

$$f(\xi) = \frac{1}{2}\rho b^d \xi^2 + Y^d \xi, \text{ for } \dot{\xi} > 0 \tag{17}$$

where $Y^d = \sigma_s H$ and $\rho b^d = \sigma_f H - Y^d$. For convenience, the critical stress level σ_s for the onset and σ_f for the completion of the detwinning deformation are introduced as material constants. Note that for the detwinning case $\dot{\xi}$ can only be positive since the unloading is entirely elastic. This adaptation of the model allows for the modelling of detwinning deformations when no stress induced martensite is being produced.

2.4 Isentropic approximation

The adiabatic heat equation can be simplified in order to facilitate the numerical treatment of the impact problem. Using the Legendre transformation (7) the internal energy can be eliminated from equation (3):

$$\rho T \frac{\partial s}{\partial t} = \pi \frac{\partial \xi}{\partial t} \tag{18}$$

Further, upon combining (6) and (10) an explicit expression for the entropy is obtained

$$s = \alpha\sigma/\rho + c\ln(T/T_R) + \Delta s_0 \xi + s_0^A \tag{19}$$

On substituting (19) into (18) the balance of energy becomes:

$$\rho c \frac{\partial T}{\partial t} = -T \frac{\partial}{\partial t}(\alpha\sigma + \rho \Delta s_0 \xi) + \pi \frac{\partial \xi}{\partial t} \tag{20}$$

According to Cory (1985) and McNichols (1987) $\pi \ll \rho \Delta s_0 T$ for most SMAs. For NiTi the precise values yield $\pi/\rho\Delta s_0 T \ll 0.013$ so equation (20) can be approximated by

$$\rho c \frac{\partial T}{\partial t} = -T \frac{\partial}{\partial t}(\alpha\sigma + \rho \Delta s_0 \xi) \tag{21}$$

which is equivalent to the isentropic condition $s_t = 0$. The heat capacity c can be assumed constant for the two phases (i.e. $c^A = c^M$). Then equation (21) can be integrated directly, yielding:

$$T = T_R e^{-\frac{1}{\rho c}(\alpha(\xi)\sigma+\rho\Delta s_0\xi)} \tag{22}$$

Consequently, the differential equation (3) is replaced by the algebraic equation (22). The impact problem then reduces to solving the balance of linear momentum (1) for the only field variable $u(x,t)$. The remaining field variables σ and T are coupled with the strain ε and the internal variable of the constitutive model ξ by equations (13) and (22).

2.5 *Tangent moduli*

A nonlinear displacement-based FEM solver utilizing the Newton-Raphson iteration to resolve the nonlinearity requires partial derivatives of the stress with respect to an increment of the strain. An increment in the strain causes increments in both stress (equation (13)) and temperature (equation (22)):

$$\frac{d\sigma}{d\varepsilon} = \frac{\partial\sigma}{\partial\varepsilon} + \frac{\partial\sigma}{\partial T}\frac{dT}{d\varepsilon} \tag{23}$$

In order to find the total derivative $\frac{d\sigma}{d\varepsilon}$ a closed form expression for $\frac{\partial T}{\partial\varepsilon}$ is needed. This is done by differentiating equations (13) and (22) with respect to the strain and combining the result to obtain:

$$\frac{dT}{d\varepsilon} = -\left(\alpha\frac{\partial\sigma}{\partial\varepsilon} + (\sigma\Delta\alpha + \rho\Delta s_0)\frac{\partial\xi}{\partial\varepsilon}\right)\Bigg/\left(\frac{\rho c}{T} + \alpha\frac{\partial\sigma}{\partial T} + (\sigma\Delta\alpha + \rho\Delta s_0)\frac{\partial\xi}{\partial T}\right) \tag{24}$$

Second order approximations for the partial derivatives $\frac{\partial\sigma}{\partial\varepsilon}$, $\frac{\partial\sigma}{\partial T}$, $\frac{\partial\xi}{\partial\varepsilon}$ and $\frac{\partial\xi}{\partial T}$ are developed in (Qidwai and Lagoudas, 2000a) and thus all the quantities in (23) can be computed numerically.

3 Numerical implementation

The numerical techniques used to implement the constitutive laws are described first. For given strain increment $\Delta\varepsilon$ and temperature increment ΔT the stress σ given by equation (13) is computed with the help of the cutting plane return-mapping algorithm described in (Qidwai and Lagoudas, 2000a). A displacement based FEM provides strain increments. In the impact problem both stress and temperature depend on the strain increment $\Delta\varepsilon$, that is for given strain both (13) and (22) have to be satisfied simultaneously. This is done via an iterative process. The process starts with given values $\varepsilon^{(0)}$, $\sigma^{(0)}$, $T^{(0)}$ for strain, stress and temperature which satisfy (13) and (22). Given a strain increment $\Delta\varepsilon$ the pair (σ, T) corresponding to strain $\varepsilon = \varepsilon^{(0)} + \Delta\varepsilon$ is found through the iteration:

$$\sigma^{(n+1)} = E\left(\varepsilon - \alpha\left(T^{(n)} - T_R\right) - \varepsilon^{t(n)}\right) \tag{25}$$

$$T^{(n+1)} = T_R e^{-\frac{1}{\rho C}\left(\alpha\sigma^{(n+1)} + \rho\Delta s_0 \xi^{(n+1)}\right)} \tag{26}$$

The first equation (25) uses the return-mapping algorithm to compute a new value $\sigma^{(n+1)}$ for the stress based on the old temperature $T^{(n)}$. The second equation (26) attempts to enforce the isentropic heat equation by computing a corrected temperature $T^{(n+1)}$. The process is terminated when there is no further progress, i.e. when $\left|\sigma^{(n+1)} - \sigma^{(n)}\right|$ and $\left|T^{(n+1)} - T^{(n)}\right|$ both become smaller than certain tolerance. The algorithm showed linear convergence in the test cases, however a detailed theoretical study is required to establish its properties.

3.1 FEM procedure

A standard semi-discrete Galerkin approximation is used to generate the weak form of the problem. In this paper only linear elements will be used. Let $P^1([0, L]) \subset H^1([0, L])$ be the set of piecewise linear functions over each element and $\{\psi_i\}_{i=1}^N$ be the usual basis of $P^1([0, L])$. The weak form of (1) then reads:

Find $u^h(x, t) = \sum_{i=1}^N U_i(t)\psi_i(x)$ such that for $\forall v^h \in P^1([0, L])$:

$$\rho \int_0^L \frac{\partial^2 u^h}{\partial t^2} v^h dx + \int_0^L \sigma \frac{\partial v^h}{\partial x} dx = -\sigma v^h \Big|_{x=0} \tag{27}$$

As usual the number of nodes is N (i.e. $N-1$ elements) and the nodal values for the displacement are denoted by $U_i(t)$. Whenever appropriate, vector notation will be used, that is $\mathbf{U} = (U_1, ..., U_N)^t$. Problem (27) is reduced to a second order nonlinear system of ODEs:

$$\mathbf{M}\ddot{\mathbf{U}} = \mathbf{F}(\mathbf{U}) \tag{28}$$

where M is the mass matrix and $\mathbf{F}_{\xi(t)}(\mathbf{U})$ is the forcing term. The subscript $\xi(t)$ stands to indicate that $\mathbf{F}_{\xi(t)}(\mathbf{U})$ does not depend on the displacement only but on the whole loading history. However, for any given loading history the stress and hence $\mathbf{F}_{\xi(t)}(\mathbf{U})$ can be viewed as well defined single valued functions. Thus, without loss of generality the subscript $\xi(t)$ will be dropped in the discussion that follows. The mass matrix and load vector are given by:

$$M_{ij} = \rho \int_0^L \psi_i \psi_j dx \tag{29}$$

$$F_i(\mathbf{U}) = -\int_0^L \sigma \frac{\partial \psi_i}{\partial x} dx \tag{30}$$

It is also useful to introduce the forcing term $\tilde{\mathbf{F}}(\mathbf{U})$ due to inelastic strains and the stiffness matrix $\mathbf{K}(\mathbf{U})$ which are given by[2]:

$$K_{ij}(\mathbf{U}) = \int_0^L E(\xi) \frac{\partial \psi_i}{\partial x} \frac{\partial \psi_j}{\partial x} dx \tag{31}$$

$$\tilde{F}_i(\mathbf{U}) = \int_0^L E(\xi) \left[\varepsilon^t(\xi) + \alpha(\xi)(T - T_R)\right] \frac{\partial \psi_i}{\partial x} dx \tag{32}$$

Note that the decomposition $\mathbf{F}(\mathbf{U}) = \tilde{\mathbf{F}}(\mathbf{U}) - \mathbf{K}(\mathbf{U})\mathbf{U}$ holds and (28) can be rewritten as:

$$\mathbf{M}\ddot{\mathbf{U}} + \mathbf{K}(\mathbf{U})\mathbf{U} = \tilde{\mathbf{F}}(\mathbf{U}) \tag{33}$$

The time integration in (28) (or (33)) is done by the backward difference method, a member of the Newmark family (Newmark, 1959; Reddy, 1993). For $t = t_s$ the Newmark scheme is defined by[3]:

$$\mathbf{U}_{s+1} = \mathbf{U}_s + \tau \dot{\mathbf{U}}_s + \frac{1}{2}\tau^2((1-\gamma)\ddot{\mathbf{U}}_s + \gamma \ddot{\mathbf{U}}_{s+1}) \tag{34}$$

$$\dot{\mathbf{U}}_{s+1} = \dot{\mathbf{U}}_s + \tau((1-\alpha)\ddot{\mathbf{U}}_s + \alpha \ddot{\mathbf{U}}_{s+1}) \tag{35}$$

The backward difference method is obtained by setting $\alpha = \frac{3}{2}$ and $\gamma = 2$. It is easy to show (see e.g. (Reddy, 1993)) that the above difference equations lead to the following system of nonlinear algebraic equations for U_{s+1}:

$$\frac{2}{\gamma \tau^2} \mathbf{M} \mathbf{U}_{s+1} = \mathbf{F}(\mathbf{U}_{s+1}) + \mathbf{G}_s \tag{36}$$

or, equivalently, to

$$\left(\frac{2}{\gamma \tau^2} \mathbf{M} + \mathbf{K}(\mathbf{U}_{s+1})\right) \mathbf{U}_{s+1} = \tilde{\mathbf{F}}(\mathbf{U}_{s+1}) + \mathbf{G}_s \tag{37}$$

---

[2] Similarly, a more precise notation for $\mathbf{K}$ and $\tilde{\mathbf{F}}$ would be $\mathbf{K}_{\xi(t)}(\mathbf{U})$ and $\tilde{\mathbf{F}}_{\xi(t)}(\mathbf{U})$, respectively.

[3] The usual notation $\mathbf{U}_s := \mathbf{U}(t_s)$ is used

where $\mathbf{G}_s = \mathbf{M}\left(\frac{2}{\gamma\tau^2}\mathbf{U}_s + \frac{2}{\gamma\tau}\dot{\mathbf{U}}_s + \frac{1-\gamma}{\gamma}\ddot{\mathbf{U}}_s\right)$. The nonlinear problem (36) is solved by linearizing the right-hand side

$$F_i(\mathbf{U} + \Delta\mathbf{U}) \simeq F_i(\mathbf{U}) + \sum_{j=1}^{N} \frac{\partial F_i(\mathbf{U})}{\partial U_j}\Delta U_j$$

and using the chain rule to obtain:

$$L_{ij}(\mathbf{U}) := \frac{\partial F_i(\mathbf{U})}{\partial U_j} = \int_0^L \frac{\partial \sigma}{\partial U_j}\frac{\partial \psi_i}{\partial x}dx = \int_0^L \frac{d\sigma}{d\varepsilon}\frac{\partial \psi_j}{\partial x}\frac{\partial \psi_i}{\partial x}dx \tag{38}$$

The solution $\mathbf{U}_{s+1}$ is found through a Newton-Raphson iterative process. Set the initial guess to $\mathbf{U}_{s+1}^{(0)} = \mathbf{U}_s$ and for $n = 1, 2\dots$ until convergence compute:

$$\mathbf{U}_{s+1}^{(n+1)} = \left(\frac{2}{\gamma\tau^2}\mathbf{M} - \mathbf{L}(\mathbf{U}_{s+1}^{(n)})\right)^{-1}\left(\mathbf{F}(\mathbf{U}_{s+1}^{(n)}) - \mathbf{L}(\mathbf{U}_{s+1}^{(n)})\mathbf{U}_{s+1}^{(n)} + \mathbf{G}_s\right) \tag{39}$$

The cutting plane method (Qidwai and Lagoudas, 2000a) which is used to resolve the nonlinear behavior of the material also provides second order numerical approximation for the derivative $d\sigma/d\varepsilon$ which results in a quasi-Newton algorithm. Since the Newton algorithm is only locally convergent in the cases when it diverges the simple iteration was applied to (37). Again, set $\mathbf{U}_{s+1}^{(0)} = \mathbf{U}_s$ and for $n = 1, 2\dots$ until convergence compute:

$$\mathbf{U}_{s+1}^{(n+1)} = \left(\frac{2}{\gamma\tau^2}\mathbf{M} + \mathbf{K}(\mathbf{U}_{s+1}^{(n)})\mathbf{U}_{s+1}^{(n)}\right)^{-1}\left(\tilde{\mathbf{F}}(\mathbf{U}_{s+1}^{(n)}) + \mathbf{G}_s\right) \tag{40}$$

In all numerical examples tested the later iteration demonstrated global linear convergence.

3.2 Adaptive mesh refinement

Let σ_n^h be the stress at the completion of the Newton iterations for given time step n, i.e. $t = t_n$. For linear elements σ^h is a piecewise constant function. Let $\overline{\sigma}^h$ be the continuous, piecewise linear function in $[0, L]$ which assumes the averaged value of σ^h at each nodal point. The error indicator $\eta_\sigma(e)$ is defined locally over each element e by (Zienkiewicz, 1987):

$$\eta_\sigma(e) = \left\|\overline{\sigma}^h - \sigma^h\right\|_{0,e} \tag{41}$$

where $\|\cdot\|_{0,e}$ is the L_2 norm. An element e is refined if

$$\eta_\sigma(e)/\sigma_{max} > TOL1 \tag{42}$$

where σ_{max} is the absolute value of the maximum attainable stress in the rod, which for impact problems is known in advance. Two neighboring elements e_i and e_{i+1} are merged into one if

$$\eta_\sigma(e_i)/\sigma_{max} < TOL2, \ \eta_\sigma(e_{i+1})/\sigma_{max} < TOL2 \tag{43}$$

Two aspects of the actual implementation details of the FE analysis should be emphasized. The linear system (36) (or (37)) is tridiagonal and poses no computational problems. Secondly, the most time-consuming parts of the FE procedure are the assembly of the stiffness matrix at each Newton step (because of the nonlinear dependance of the stiffness on the strain) and the assembly of the force vector. They require the execution of the stress update procedure via the return-mapping algorithm which is a computationally expensive operation and is preformed once for each element at each Newton step.

Clearly a global uniform h-refinement strategy used to achieve satisfactory spatial discretization will impose severe restrictions on the problem size due to the assembly time issues. In order to avoid this the local criterion (42) is applied to each element at the completion of the Newton iteration to refine or coarsen the mesh. If there is no further need to refine the mesh the algorithm proceeds to the next time step. It was found that this approach works very well for the class of SMA hysteretic materials under consideration.

4 Numerical Examples

The implementation of the FEM was tested in three different numerical examples. The step loading problem under conditions of pseudoelasticity ($T > A^{of}$) presented in the next section is used to compare the numerical solution to existing analytical solutions (Chen and Lagoudas, 2000; Bekker et al., 2002). It is also used to demonstrate the capabilities of the adaptive mesh refinement strategy. Secondly, a problem with pulse boundary conditions is solved, again under pseudoelastic conditions. The third problem also features a pulse boundary condition but at a lower temperature ($T < M^{os}$) so only detwinning of martensite is involved.

The material properties (Table 1) for all model problems are taken from (Qidwai and Lagoudas, 2000a) and represent generic NiTi SMA properties. In addition to that for all numerical simulations the length of the rod was taken to be 0.5m. All calculations were performed on a 933 Mhz PIII machine running Windows NT.

Table 1
Material parameters used in the SMA model

Material constant	Value	Material constant	Value
E^A	70×10^9 Pa	$\frac{d\sigma}{dT}$	$7.0 \times 10^6\ Pa/(m^3K)$
E^M	30×10^9 Pa	M^{of}	275 $^\circ K$
α^A	$22 \times 10^{-6}/K$	M^{os}	291 $^\circ K$
α^M	$10 \times 10^{-6}/K$	A^{os}	295 $^\circ K$
H	0.05	A^{of}	315 $^\circ K$

4.1 Step loading problem

The fixed impact stress initial-boundary value problem[4] is defined by setting the boundary condition to be the step function:

$$\sigma_0(t) = \begin{cases} 0 & \text{for } t \le 0 \\ \sigma_0 & \text{for } t > 0 \end{cases} \tag{44}$$

The strain level ε_0 which causes the constant impact stress σ_0 can be found from equation (13). This particular boundary condition is chosen because it is a natural starting point for nonlinear hyperbolic equations and because there are existing analytical solutions for it.

4.1.1 Analytical solutions to the step loading problem

The structure of the solution depends strongly on the impact stress σ_0. Let the pair $(\varepsilon_{el}, \sigma_{el})$ be the point on the hysteresis curve that corresponds to the start of the phase transformation. In this example σ_0 it is taken to be sufficiently high so that full phase transformation transformation has occurred. It is also required that the value of σ_0 be high enough, so that the graph of of the stress strain relationship of the SMA is below the line connecting the points $(\varepsilon_{el}, \sigma_{el})$ and $(\varepsilon_0, \sigma_0)$ (see Figure 1).

Following Chen and Lagoudas (2000); Bekker et al. (2002) it can be shown that for material with initial linear stress-strain relationship prior to the onset of phase transformation the solution has the following two-shock structure:

---

[4] When the same initial boundary value problem is reformulated as an initial problem on an infinite domain with the initial condition being a step function it is usually referred to as the *Riemann* problem.

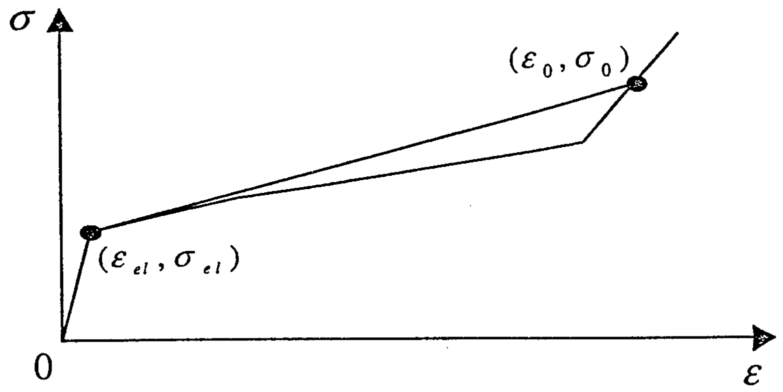
σ
$(\varepsilon_0, \sigma_0)$
$(\varepsilon_{el}, \sigma_{el})$
0
ε

Fig. 1. Schematic of the loading portion of a stress-strain relationship and the critical points defining the solution to the problem.

$$\sigma(x,t) = \begin{cases} \sigma_0 \text{ for } 0 \le x/t \le V_{ph} \\ \sigma_{el} \text{ for } V_{ph} < x/t \le V_{el} \\ 0 \text{ for } V_{el} < x/t \end{cases} \tag{45}$$

$$T(x,t) = \begin{cases} T_0 \text{ for } 0 \le x/t \le V_{ph} \\ T_{el} \text{ for } V_{ph} < x/t \le V_{el} \\ 0 \text{ for } V_{el} < x/t \end{cases} \tag{46}$$

where T_0 is the temperature corresponding to the impact stress σ_0 and T_{el} is the temperature just prior to the onset of the phase transformation. The faster shock is a linear thermoelastic elastic shock and has velocity

$$V_{el} = \sqrt{\frac{\sigma_{el}}{\rho\varepsilon_{el}}} \tag{47}$$

This shock is due to the shock type of the boundary condition and the initial linear stress-strain response. The second, slower shock, is a transformation shock which travels with velocity

$$V_{ph} = \sqrt{\frac{\sigma_0 - \sigma_{el}}{\rho(\varepsilon_0 - \varepsilon_{el})}} \tag{48}$$

This shock occurs not only because of the boundary condition but also because of the convex-down nature of the stress-strain relationship for $\varepsilon > \varepsilon_{el}$. Higher stress levels travel with higher velocity than lower stress levels which make the shock self sustained and independent of the boundary condition (see (Godlewsky and Raviart, 1996, pg. 83-97) for a general discussion as well as (Chen and Lagoudas, 2000; Bekker et al., 2002) for solutions specific to SMA materials). The phase transformation shock specifies the point of abrupt phase transition. For material points with $x \leq V_{ph}t$ the material is in the martensitic phase and the region $x \geq V_{ph}t$ is still in the austenitic phase.

Note that the adiabatic heat equation (22) does not provide for a completely linear initial response. However, prior to the onset of phase transformation, $\xi = 0$ and the heat equation (22) can be linearized as follows:

$$T = T_R(1 - \frac{\alpha}{\rho c}\sigma) + \mathcal{O}\left((\frac{\alpha\sigma}{\rho c})^2\right) \tag{49}$$

By neglecting the higher order terms in (49) the remaining linear part can be substituted in (13) to obtain a completely linear adiabatic stress-strain response. The linear approximation in (49) is justified in the thermoelastic range before commencement of phase transformation because $\frac{\alpha\sigma_0}{\rho c} \approx 10^{-3}$. If equation (22) is not linearized the elastic shock will be replaced by a continuous function with very high gradient. The velocity of the points on the graph of this function will deviate from the velocity V_{el} of the elastic shock by $\approx 10^{-5}$.

4.1.2 Numerical results for the step loading problem

For all numerical simulations the impact stress level is $\sigma_0 = -400 MPa$ corresponding to impact strain of $\varepsilon = 0.0635$. The reference temperature is $T_R = 320\ ^\circ K$. The FEM solver was set to use the backward difference time integration scheme and the Newton-Raphson method to solve the nonlinear system (36). The Newton-Raphson iteration showed quadratic convergence at all time steps except for the first few ones when the shock were forming. In the cases when it was diverging the alternative direct iteration (40) approach was used.

Significant computational savings can be obtained if isothermal instead of adiabatic conditions are assumed. In an *isothermal* problem the temperature is held constant $T = T_R$ and the balance of energy (2) is not considered. Thus the quasi-static hysteresis of the material is used instead of solving equations (13) and (22). For a NiTi SMA with the material data from Table 1 the difference between the adiabatic and isothermal hysteresis is shown in Figure 2. The shape of the hysteresis is the same and the differences in the transformation portion will not affect the structure of the solution provided that σ_0 is well above the stress level required to finish the transformation. Consequently, no matter whether isothermal or adiabatic conditions are assumed the shock speeds V_{ph} and V_{el} will only depend on the values for ε_{el}, σ_{el}, ε_0, σ_0. From a computational point of view this simplification avoids the iteration process

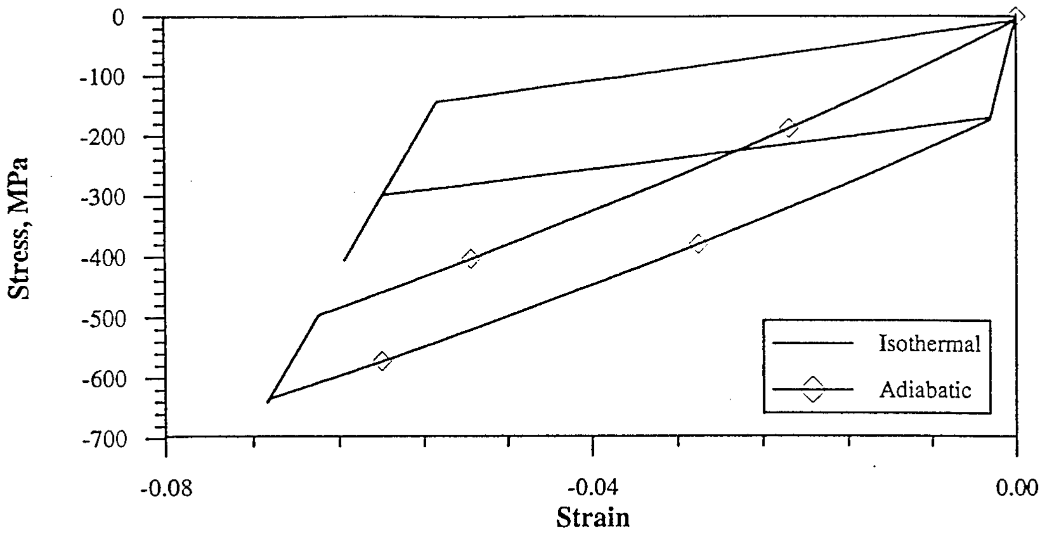

Fig. 2. An adiabatic and isothermal path for the material data in Table 1 at $T = 320\ ^\circ K$. Under adiabatic conditions higher stress levels are required to complete the phase transformation compared to isothermal hysteresis loops.

(25),(26) (typically 6-7 iterations) which results in a significant reduction in computational time. While the structure of the solution is not compromised very fine spatial meshes can be explored for the purposes of comparing analytical and numerical solutions.

For the isothermal hysteresis (Figure 2) an impact stress of $\sigma_0 = 400MPa$ is sufficient for the full completion of the phase transformation under isothermal conditions. The onset of phase transformation begins at $\sigma_{el} = -195MPa$ for a strain $\varepsilon_{el} = 2.78 \times 10^{-3}$. Given this, the speed of the two shocks (48) and (47) are found to be:

$$V_{ph} = 723m/s \tag{50}$$
$$V_{el} = 3294m/s \tag{51}$$

Based on the first few numerical results (Figure 3) and (Figure 4) several observations can be made. First, all numerical solutions have the expected two shocks - one elastic and another corresponding to the phase transformation. Fixed meshes with coarse spatial discretizations have oscillations close to the phase shock location. A comparison of the two meshes in Figure 3, both for a fixed time-step of $\tau = 0.1\mu s$ at time $t = 30\mu s$ shows that oscillations can be eliminated by refining the mesh. Secondly, the backward difference scheme which was used in these computations, introduced numerical dissipation which is most pronounced at the elastic shock. Several other members of the Newmark family were tested. Explicit methods as well as the constant acceleration scheme were found to be unconditionally unstable producing highly oscillatory solutions that were diverging with time. Of those methods that were able to converge the backward difference was found to dampen the high frequency

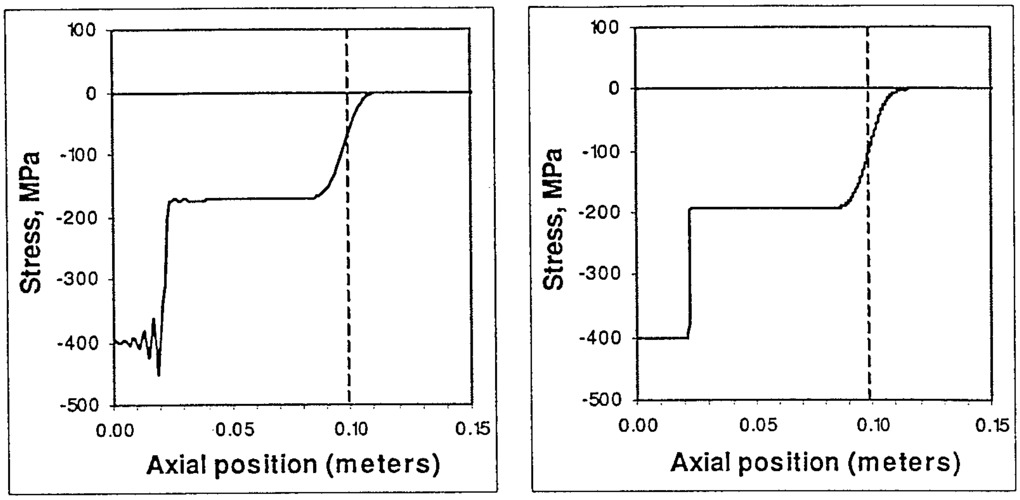

(a) (b)

Fig. 3. Stress profile at $30\mu s$ for a fixed mesh with 500 (a) and 2000 elements (b). Numerical oscillations are eliminated for the finer spatial discretization. The position of the elastic shock is marked by a dashed line.

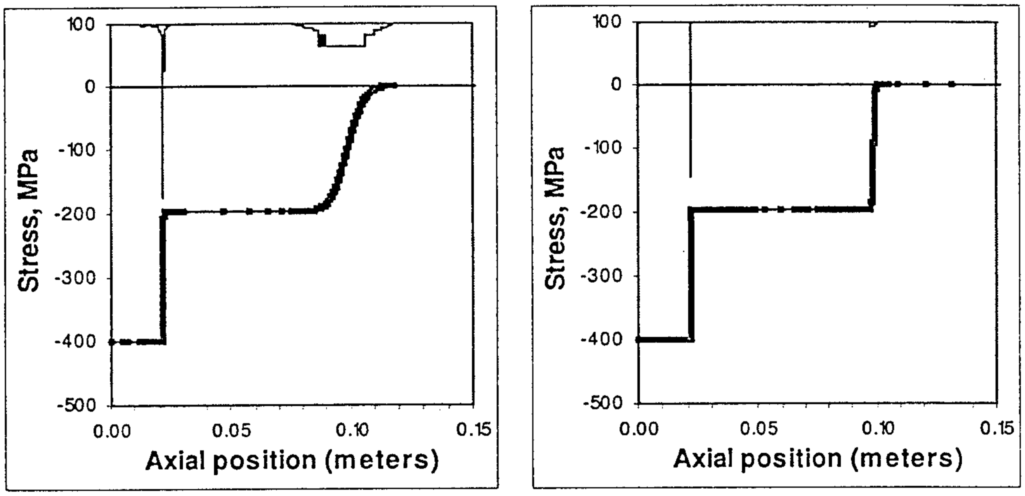

(a) (b)

Fig. 4. Stress profile at $30\mu s$ for an adaptive mesh with two different time steps. The linear shock is smeared for a coarse time step $\tau = 0.1\mu s$ (a). It is much sharper when a finer step of $\tau = 0.001\mu s$ (b) is used. Mesh nodes are marked with black squares and the thin line at the top shows the density of elements.

oscillations (Figure 3(a)) in the most efficient manner and was subsequently chosen for all future computations. The numerical dissipation can be decreased by appropriately decreasing the time step. The quasi-Newton method used to solve the nonlinear system (36) showed quadratic convergence at all time steps but the first few ones when the shock were forming. In that case the alternative direct iteration (40) approach was used.

Quantitatively the results obtained by both the fixed and adaptive FEM are in agreement with the analytical solution. In regions away from the shocks the relative difference in the values of the stress for the numerical and the exact solution is less then 10^{-4}. The accuracy of the solutions therefore is determined based on the quality of the numerical solution close to the shock locations. The interval covering a shock (phase or elastic) where the numerical values for the stress differ from the exact ones by more than 1% is assumed to be the range of uncertainty for the numerical value of the shock location. Consequently, the left and right end of this interval are assumed to be bounds for the position of the shock of the numerical solution.

Based on this measure of error, for a time step of $\tau = 0.1\mu s$ the phase shock is found to travel with velocity in the range $693 - 900 m/s$. The velocity of the elastic front is calculated to be in the range $3316 \pm 420 m/s$. These results are the same for a fixed (Figure 3(b)) and adaptive mesh (Figure 4(a)). This indicates that the adaptive and fixed FEM converge to the same solution.

The smearing of the stress profile in the region of the elastic shock is due to the time-integration scheme. When the time step is decreased the slope becomes steeper and eventually converges to the shock. For an adaptive solution with a time step $\tau = 0.001\mu s$ (the same computation for a fixed mesh was time prohibitive) the calculated values for the phase shock are now in the range $723 - 733 m/s$ and the elastic shock is within the bounds $3256 - 3366 m/s$ (Figure 4(b)). This indicates that the lower bound for the transformation shock is very close to the actual value (50) and that the elastic shock (51) is virtually in the middle of the suggested numerical range. The relative error in the predicted value for the phase shock velocity decreases from 24% for $\tau = 0.1\mu s$ down to 1.3% for $\tau = 0.001\mu s$. The error in the elastic shock speed decreases from 12% to 1.1% which is a clear indication that the FEM algorithm is converging to the exact solution.

An inspection of Figure 3 reveals that there are large regions in the bar with no variation in the stress. This is fully utilized by the adaptive approach. Figure 4(a) shows an adaptive FE solution with the same time step as the solution on Figure 3(b) and a adaptive tolerance (see (42)) set to 10^{-4}. This accuracy is comparable to the one of a fixed mesh with 2000 elements. The maximum number of elements that the adaptive mesh contained was 305. The order of magnitude fewer number of elements in the adaptive meshes induced a corresponding order of magnitude decrease in the computational time.

A comparison in the performance of the fixed and adaptive FE methods is given in Table 2. The time step is $\tau = 0.01\mu s$. The number of elements for the fixed FEM is 16000. The adaptive solution was chosen so that it had compa-

Table 2
Execution times for fixed and adaptive meshes

Time	Fixed Mesh		Adaptive Mesh	
	Elements	Time (min)	Elements	Time (min)
10 μs	16000	56	161	1:12
20 μs	16000	113	199	2:37
40 μs	16000	226	256	6:10
80 μs	16000	451	301	15

rable accuracy with the one for the fixed mesh solution. A comparison of the execution times for the fixed and adaptive methods shows that the adaptive procedure delivers an order of magnitude improvement in performance.

4.2 Square pulse loading problem in pseudoelastic conditions

A more realistic initial-boundary value problem is one for which, instead of step loading, the boundary condition is a square pulse, that is

$$\sigma_0(t) = \begin{cases} 0 & \text{for} \quad t \leq 0 \\ \sigma_0 & \text{for} \quad 0 < t < t_{pulse} \\ 0 & \text{for} \quad t \geq t_{pulse} \end{cases} \tag{52}$$

where t_{pulse} is the duration of the pulse. Due to the complicated constitutive response and boundary conditions there is no analytical solution to be compared with. Moreover, there are unresolved questions regarding the uniqueness of the weak solution for times $t > t_{pulse}$ when unloading takes place.

The stress level used for the numerical simulation is $\sigma_0 = 800 MPa$ and the initial temperature is $T_R = 320\ ^\circ K > A^{of}$. The simulation is done for adiabatic conditions, utilizing both equations (13) and (22) to calculate the adiabatic response of the SMA. The stress level is chosen so that the full adiabatic hysteresis loop can be realized (see Figure 2). The pulse length is $t_{pulse} = 10 \mu s$ and the time step is $t = 0.001 \mu s$.

The evolution of the stress and temperature in the rod up to $90 \mu s$ is shown in Figures 5 and 7. As predicted by (45) the two-shock solution for the stress is clearly visible at the end of the pulse load at $t = 10 \mu s$ (Figure 5). The temperature profile (Figure 7) also has two shocks (equation (46)). The maximum temperature $T_0 = 378.8\ ^\circ K$ is achieved in the region of full phase transforma-

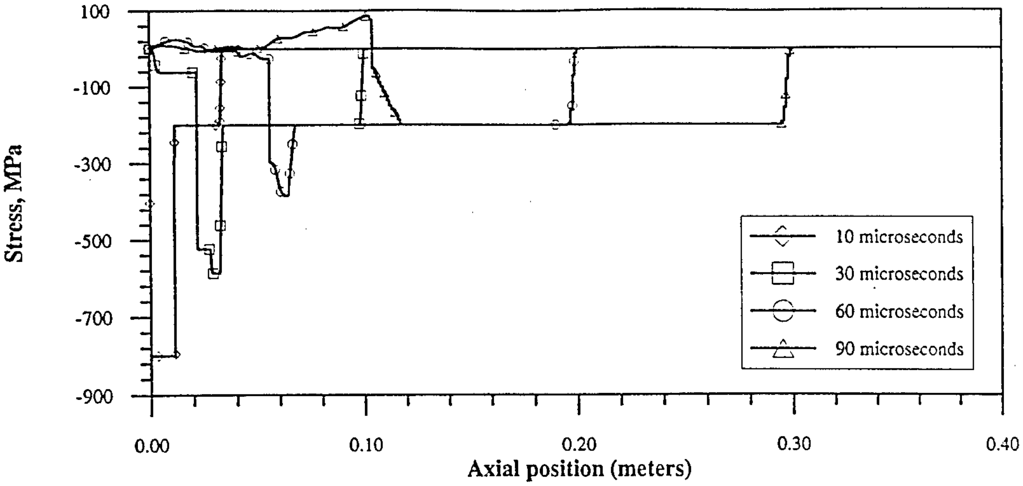

Fig. 5. Stress profile at different instances of time for a square pulse in adiabatic loading

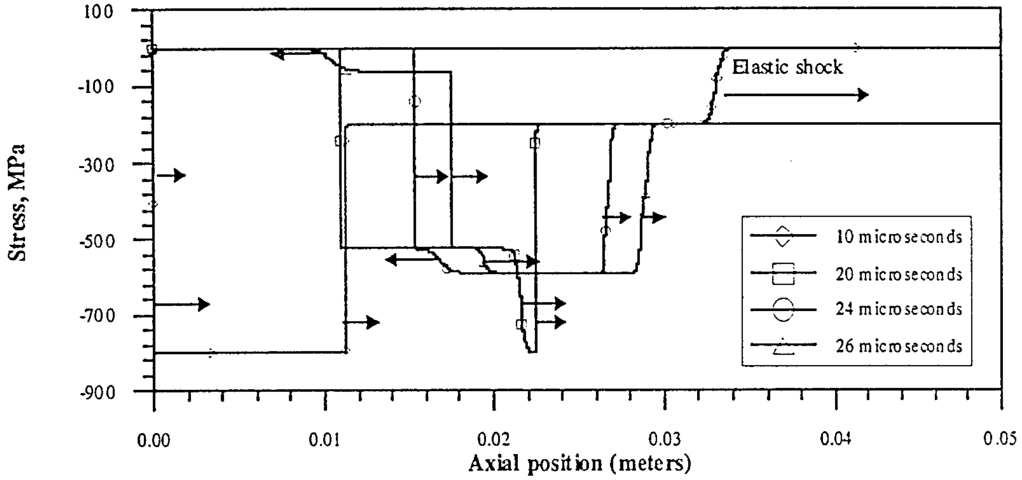

Fig. 6. Magnified view near the left end. The unloading ($10\mu s$) produces two right-travelling shock waves ($20\mu s$). The faster unloading wave reflects off the transformation shock ($\approx 21\mu s$) and forms a left-travelling wave ($24\mu s$). What follows is a series of complicated reflections that gradually kill the initial non-linear shock.

tion. The jump in the elastic shock is $T_{el} - T_R = 0.66\ ^\circ K$ and for this reason it is not clearly visible in the figure.

The most noticeable feature observed in Figure 6 is the structure of the unloading pulse. Again a two wave shock structure is seen that corresponds to the initial elastic unloading and the following reverse transformation $M^t \to A$ as can be seen from the stress profile at 10 and $20\mu s$. Both unloading shocks travel faster than the forward phase transformation shock. When the faster unloading front catches up with the forward phase transformation shock ($t \approx 22\mu s$) a left-travelling reflection is generated. The left-travelling wave, as seen for $t = 24\mu s$, partially reflects from the slower unloading shock and partially continues ($t = 26\mu s$) until it reflects off the left end of the rod. A complicated

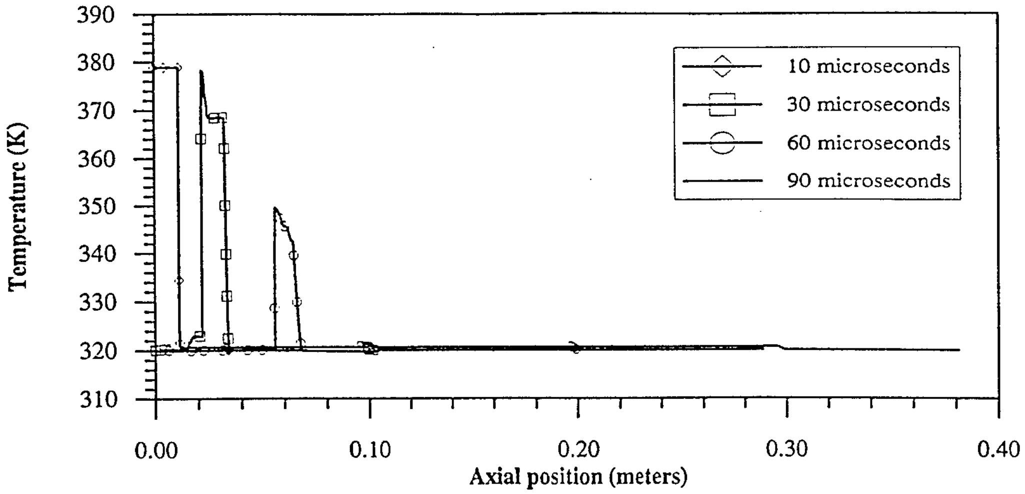

Fig. 7. Temperature profile at various times. The jump at the forward transformation shock is $T_0 - T_{el} = 58.2\ ^\circ K$. The elastic shock is not visible clearly because of its small magnitude of $T_{el} - T_R = 0.66\ ^\circ K$.

series of reflection waves follows. The first reflection results in approximately 34% decrease of the peak stress level ($t = 24\mu s$). The picture becomes even more complicated when the slower unloading shock eventually catches up with the forward travelling phase transformation shock. Eventually the peak stress levels are reduced to values below σ_{el}, the critical stress corresponding to the onset of phase transformation. The temperature profile at $t = 90\mu s$ is hardly visible because the material is entirely in the elastic range and the temperature in the rod is very close to the reference temperature. The large amounts of latent heat generated during the initial loading phase are gradually consumed in the reverse transformation as the stress is reduced within the elastic limits.

For pulse loading it is physically meaningful to compute the energy dissipation due to the phase transformation. If $P(\tau)$ is the work done by the external forces at the left end of the rod from $t = 0$ up to $t = \tau$, $\mathcal{K}(\tau)$ is the kinetic energy of the rod at time $t = \tau$ and $\mathcal{W}(\tau)$ is the stored elastic energy of the rod then the energy dissipation is defined by

$$D(\tau) = \frac{P(\tau) - (\mathcal{K}(\tau) + \mathcal{W}(\tau))}{P(\tau)} \qquad (53)$$

The quantities P, $\mathcal{K}$ and $\mathcal{W}$ given by

$$\begin{aligned} P(\tau) &= \int_0^\tau \sigma(0,t) v(0,t) dt \\ \mathcal{W}(\tau) &= \tfrac{1}{2} \int_0^L \sigma(x,\tau) \varepsilon^e(x,\tau) dx \\ \mathcal{K}(\tau) &= \tfrac{1}{2} \int_0^L \rho (v(x,\tau))^2 dx \end{aligned} \qquad (54)$$

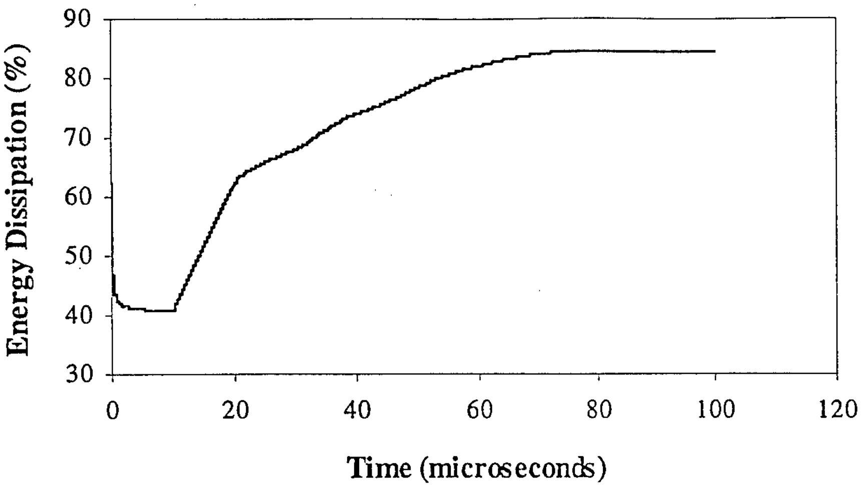

Fig. 8. Energy dissipation for a 10 μs square pulse in adiabatic conditions.

can be easily computed numerically at each time step.

The calculations show (Figure 8) that the dissipation level goes from 40% at the end of the pulse ($T = 10\mu s$) to 64% at $T \approx 22\mu s$ when the faster unloading wave reflects off the forward travelling transformation wave. The high stress levels are then gradually reduced within the elastic limits. The energy dissipation reaches approximately 84% at 100 μs, shortly before the elastic front reaches the right end.

4.3 Detwinning Induced by a pulse load

In this numerical simulation the same boundary condition (52) as in the previous section is used. The initial temperature is set to $T_R = 295\ ^\circ K$ which is in the detwinning range and the material is initially in the M^t state. The stress pulse has magnitude $\sigma_0 = 400MPa$ which is sufficient to complete the detwinning and then obtain the elastic response of the martensite phase.

There is no latent heat generation during the detwinning deformation. If it is assumed that all the work dissipated through inelastic deformations is transformed into heat, then the change in temperature would be $\approx 2\ ^\circ K$. Therefore it is both physically and computationally justified to perform the simulation in an isothermal setting. The loading part of the hysteresis is of the same type as the loading part ($A \to M^d$) of the stress-strain relationship for stress induced martensite. Therefore for the duration of the pulse a two-shock structure for the stress distribution can be expected (see equations (45), (50) and (51)). This is observed clearly for the stress profile at $t = 10\mu s$ in Figure 10.

The unloading is completely elastic and a single linear shock forms, travelling

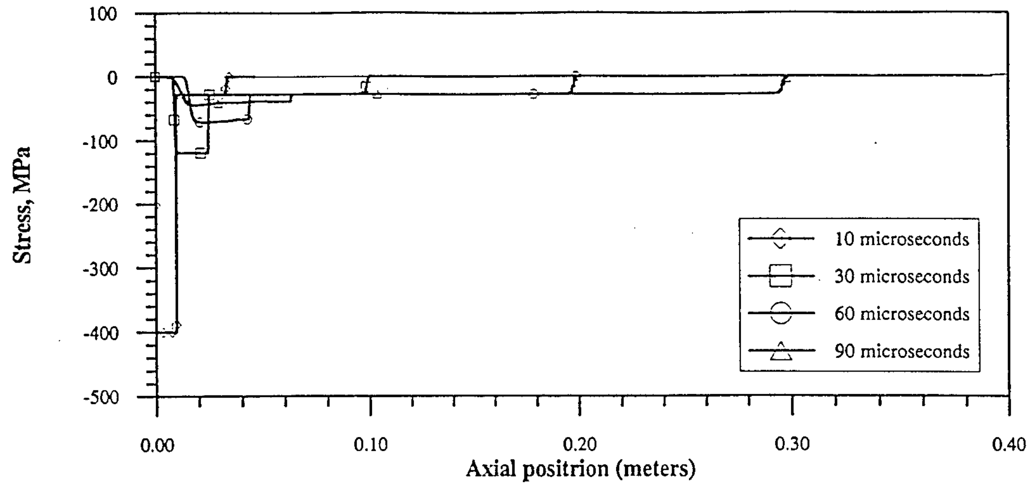

Fig. 9. Stress profiles at various times for a square pulse. The material is the detwinning range. The attenuation of the stress to values within the elastic material response is clearly visible.

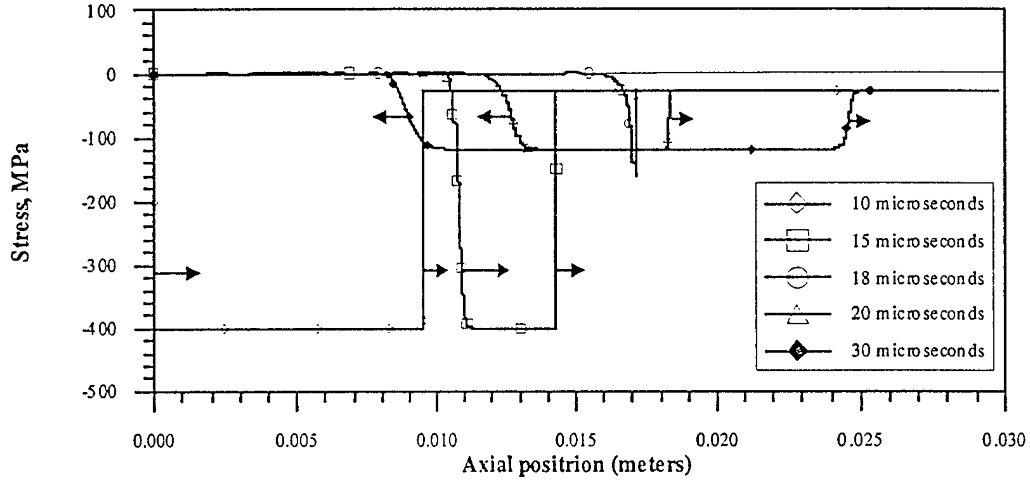

Fig. 10. Magnified view of stress profiles in the region close to the left end of the rod. Direction of the shock velocities are indicated by arrows.

at the speed of the forward elastic shock (both the initial loading response and unloading are linear with the elastic modulus of martensite). The unloading shock is therefore fast enough to catch up with the nonlinear shock caused by the detwinning. This is followed by a series of reflections between the left end (which is traction free after the pulse is over) and the forward propagating detwinning shock. The stress profile at several different instances of time is presented in Figure 9.

The energy dissipation (Figure 11) in the rod follows a similar path as in the previous numerical simulation. The first significant rise in the dissipation levels occurs immediately after unloading, at $t = 10\mu s$. After the unloading wave reaches the forward propagating detwinning front at $t \approx 18\mu s$ a new rise in the dissipation occurs leading to final levels of approximately 86%. It should

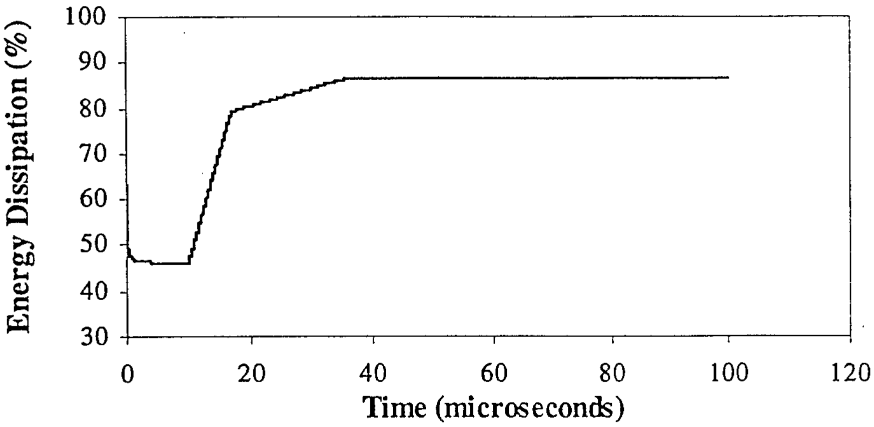

Fig. 11. Energy dissipation for a 10 μs square pulse.

be noted that this case is not equivalent to the pulse load in pseudoelastic conditions because of different initial stress levels. Another difference with the pseudoelastic case is that the material is permanently deformed and in order to recover its shape the rod has to be reheated.

5 Dynamic Loading Experiment of an SMA rod

The dynamic response of a nearly equiatomic NiTi alloy rod is characterized with one dimensional wave propagation experiments in a Hopkinson bar arrangement. The main feature of the Hopkinson implementation of the dynamic experiment is in the length of the specimen, L_{sp} which is quite long. This means that a steady-state condition is not reached during the time of the experiment and one has to deal with the propagation of the wave in the specimen material.

5.1 Description of the Apparatus

Hopkinson bar apparatus has become standard in the characterization of the dynamic response of materials. Detailed descriptions are provided in many handbooks and textbooks (Kolsky, 1963; Graff, 1975), and hence only a brief description is provided here. A photograph of the experimental setup is shown in Figure 12 and a schematic of the impact device is given in Figure 13.

The apparatus consists of a striker bar, an input bar and an output bar, all of diameter $d = 15.5mm$ and all made of a 4340 steel, quenched and tempered to a martensitic state. The yield strength of these bars is about 1.8 GPa and they remain elastic during the impact experiments. The density of the bars is

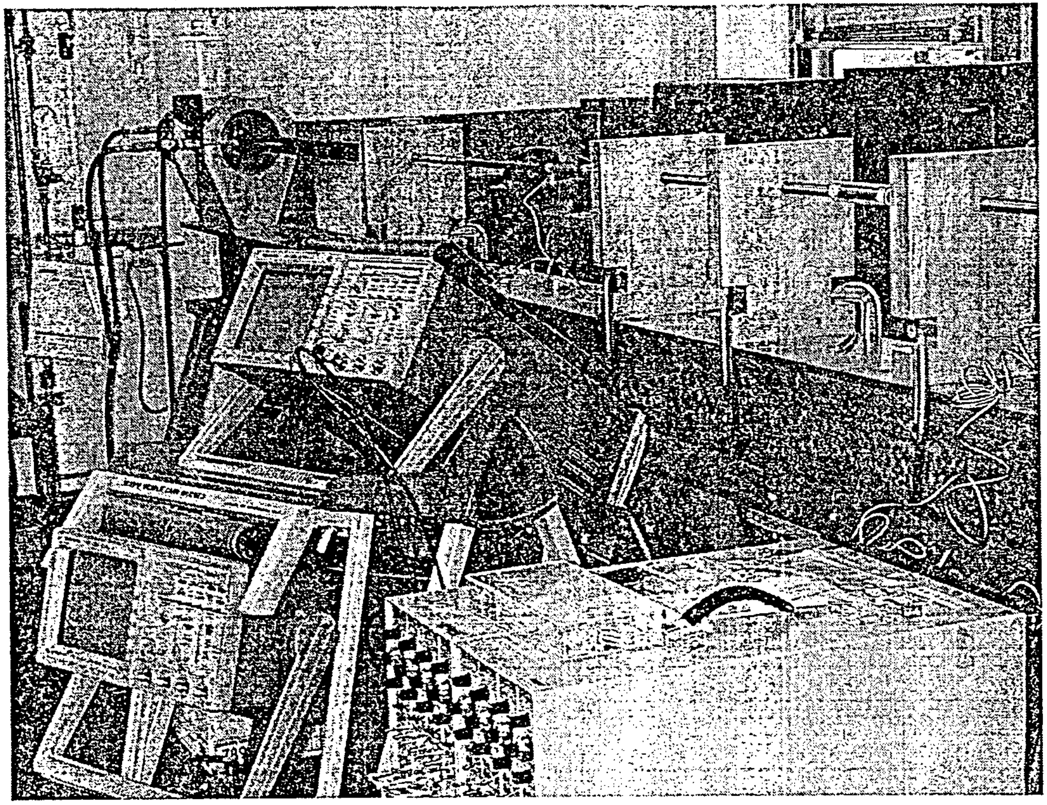

Fig. 12. Photograph of the Hopkinson bar experimental setup. The specimen is visible at the top-right part of the photograph

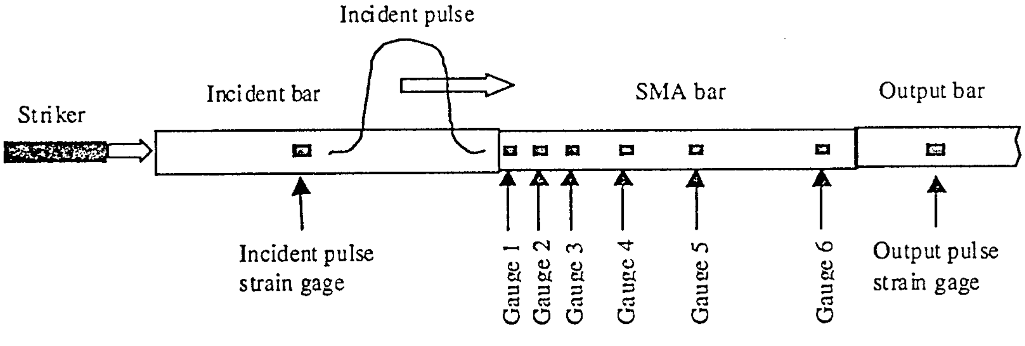
Incident pulse
Striker
Incident bar
SMA bar
Output bar
Incident pulse strain gage
Gauge 1
Gauge 2
Gauge 3
Gauge 4
Gauge 5
Gauge 6
Output pulse strain gage

Fig. 13. Geometry and arrangement of strain gauges in Hopkinson apparatus. (Figure not drawn to scale)

$\rho = 7800 kg/m^3$, the measured bar wave speed $C_b = \sqrt{E_b/\rho} = 5300 m/s$ and E_b is the modulus of elasticity of the steel bar. The striker bar (13) of length L is propelled from an air gun at speeds in the range of 10 to 40 m/s. This striker impacts the input bar which is $1.7m$ long. A one dimensional compression wave propagates into both bars. Since the striker bar is short, the reflected tension pulse arrives at the striker-input bar interface at a time $t_{pulse} = 2L/C_b$. At this point, the striker comes to a stop and is disengaged from the input bar. Hence, a compression pulse of duration t_{pulse} is propagated down the length of the input bar. This wave is coupled into the specimen which is in contact with the far end of the input bar. Due to the impedance mismatch between the specimen and the input bar, part of the pulse is reflected back into the input bar and part of the pulse propagates into the specimen. A strain gauge mounted at about the middle of the input bar is used to monitor the incident compressive pulse and the reflected tensile pulse propagating in the input bar. The wave propagating through the specimen, gets coupled into the output bar, again with a reflected component due to the impedance mismatch. The output bar is free at the far end and so a tensile pulse reflects from the far end of the output bar and is unable to transmit into the specimen. Hence the specimen is loaded only once. A strain gage mounted at the middle of the output bar is used to monitor the strain pulses, in particular the first transmitted pulse, in the output bar.

5.2 Specimen Preparation

In the experiments a single SMA specimen 345 *mm* long was used as well as two short specimens of 25.4 *mm* length. All the specimens had diameter 12.7 *mm*. After machining the specimens to the appropriate lengths they were heated to 540 °*C* in standard atmosphere for 2 hours and furnace cooled. This process was used to erase history of prior plastic deformation. A thin oxide layer was formed during the heat treatment, but this did not affect the overall response of the material. In the long bar, six strain gauges were placed at distances 10 *mm*, 20 *mm*, 40 *mm*, 80 *mm*, 160 *mm* and 320 *mm* from the impact end. A high temperature strain gauge adhesive was used and the specimens were then annealed at 100 C for 1 hour. Subsequently, the specimens were cooled to dry ice temperature (-70 °*C*) and then brought to room temperature for testing. All tests were performed at room temperature (nominally 20 °*C*). A Differential Scanning Calorimeter (DSC) was used to determine the transformation temperatures in the material. As can be seen from the DSC measurements shown in Figure 14, under the indicated temperature cycling, the specimens were in a twinned martensitic state during the tests. In order to obtain preliminary information on the mechanical behavior of this material quasi-static compression test was performed on one of the short specimen in a standard testing machine. Since the dynamic test involved only detwinning of martensite the quasi-static tests were done at room temperature. These tests were used to obtain the stiffness of the martensitic phase E^M and the critical stresses σ_s and σ_f for onset and finish of detwinning.

The material constants used for the detwinning model are summarized in Table 3. The hysteresis simulated by the model (Section 2.3) and the actual hysteresis from the quasi-static test are given in Figure 15.

Table 3
Material parameters used in the SMA model for detwinning

Material constant	Value	Description
E^M	42×10^9 Pa	Modulus of elasticity in martensite
H	0.027	Maximum detwinning strain
σ_s	-125MPa	Start of $M^t \to M^d$ deformation
σ_f	-273MPa	Completion of $M^t \to M^d$ deformation
Y^d	$\sigma_s H$	
ρb^d	$\sigma_f H - Y^d$	

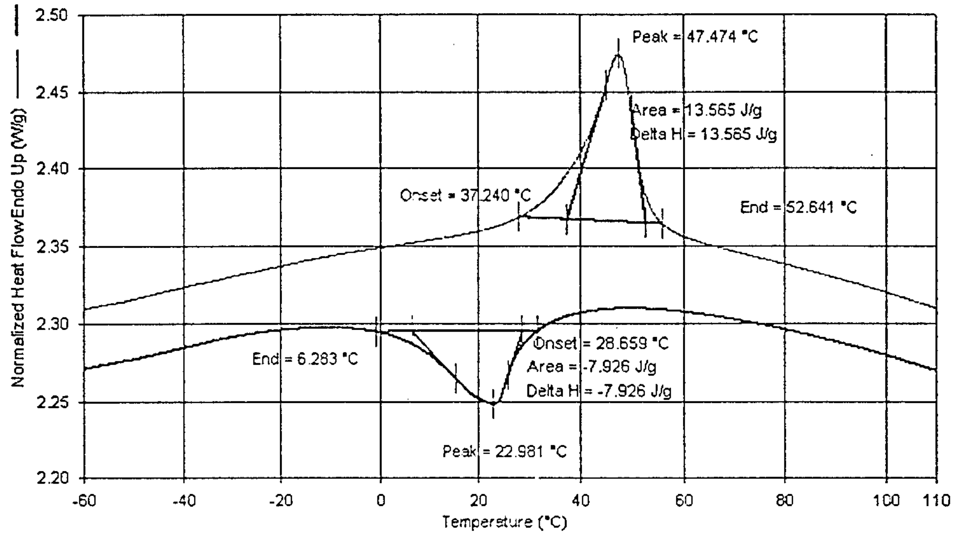

Fig. 14. Differential Scanning Calorimeter measurements of the SMA specimen.

5.3 Dynamic Results

As indicated earlier, in the Hopkinson bar experiment a 345 *mm* long rod instrumented with six strain gauges was placed behind the input bar. The output from these gauges is shown in Figure 16. Strain gauge number 3 (40*mm*) suffered a partial debond during the test and hence the results from this gauge are not meaningful beyond the point marked by the dark dot in the figure. The elastic wave in the input bar was not recorded due to an error in the device; all other gauges worked well and recorded the strain profile as the wave propagated down the length of the SMA rod. An x-t diagram corresponding to elastic wave propagation in this specimen is shown in Figure 17. The strain gauge locations are indicated by the thin vertical lines and the leading edge of the initial loading pulse is shown by the dark line; this pulse reaches each one of the gauges at the time where the dark line intersects the vertical lines. From the timing of the elastic wave arrival at each gauge, the elastic wave speed was determined to be 2500 m/s. The elastic wave reaches the far end

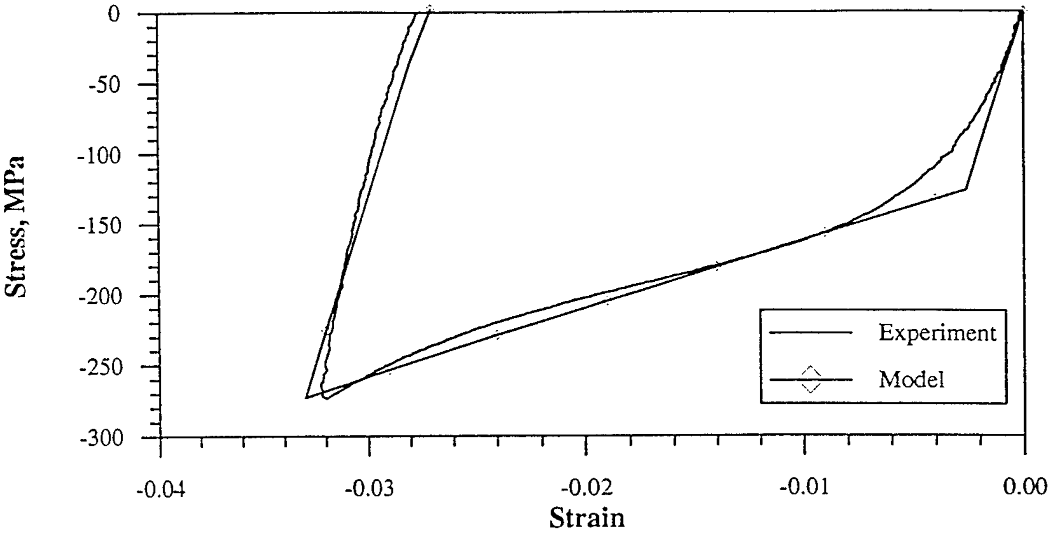

Fig. 15. Quasi-static hysteresis of SMA specimen and the model simulation.

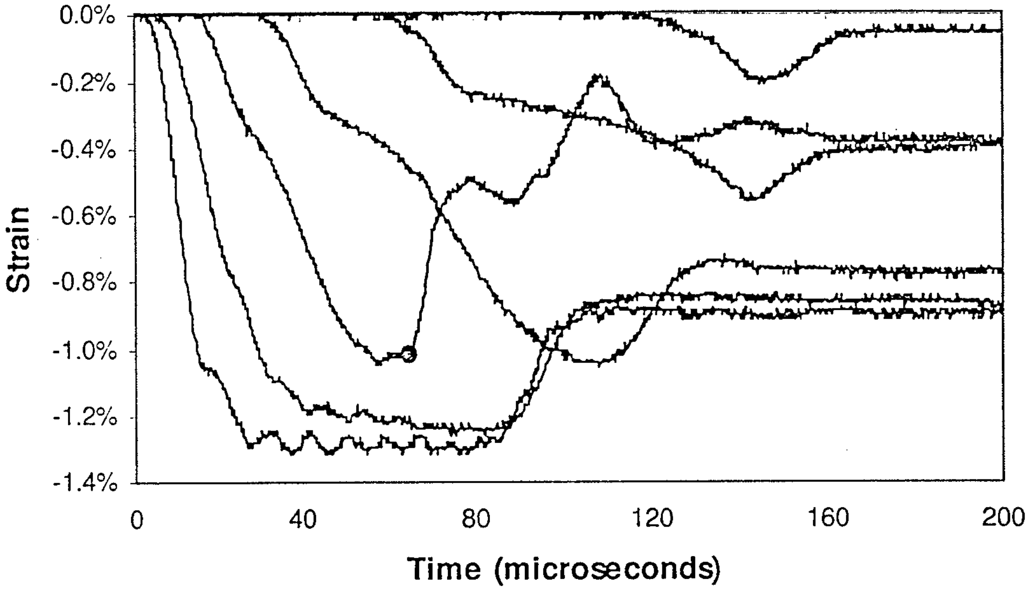

Fig. 16. Strains measured by the gauges mounted on the SMA bar. Gauge 3 suffered a partial debond at the point indicated by the dark circle and hence the data beyond this time should not be interpreted.

of the specimen about 138 μs after impact. The duration of the loading pulse is about 90 μs and hence an unloading pulse propagates from down the specimen with the elastic wave speed (since the unloading is elastic). This wave is shown by the line with an arrow at the tip. Time $t = 0$ corresponds to the first arrival of the loading pulse at the strain gauge in the input bar.

As seen in Figure 16, the strain in the first two gauges increases rapidly to a level of about 1.3% and levels off as the load from the input bar levelled

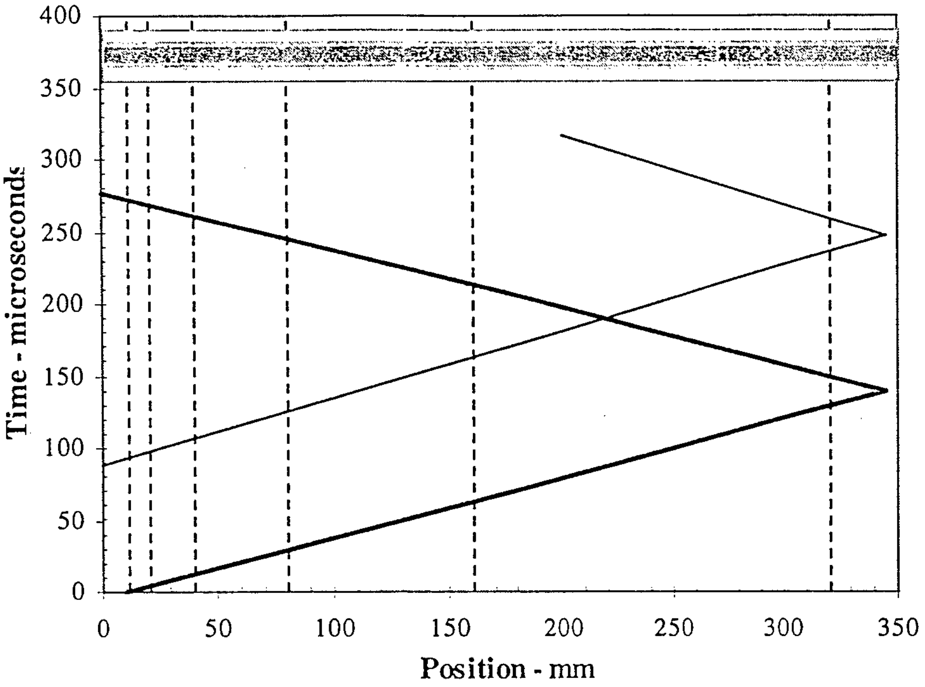

Fig. 17. X-t diagram indicating arrival of the elastic wave front at the gauge locations.

off. The oscillations seen in these gauges near the plateau are Pochhammer-Chree oscillations that appear in bars. At around 290 μs the unloading wave from the end of the loading pulse reaches the first two gauges and the strain begins to decrease; however, because the strains beyond 0.3% were the result of detwinning (see the quasi-static results in Figure 15), these strains are not recovered and a permanent strain of about 1% is left at these locations. The signal in gauge 4 clearly indicates the dispersion of the wave - higher strain levels propagate at significantly slower speeds and arrive later at the gauge location. Hence a broadening of the strain pulse can be seen - the peak in the strain at gauge 4 occurs 75 μs after elastic wave arrival while it occurs in about 20 μs in gauge 1. This delay also results in the peak strain not being sustained for too long as the elastic unloading pulse reaches the gauge quickly; once again a residual strain of peak strain - 0.3% is left at this gauge location. The same behavior is seen in gauge 5 where due to its distance from the impact end, and due to the slowness of the inelastic waves, the peak strain reached is only about 0.5%. Once again a residual strain is left in this location. In gauge 6, the reflected wave from the end of the SMA rod (left free in this experiment) causes unloading of the gauge; a very small, but measurable permanent strain or detwinning is observed in this location. Subsequent to the test, the rod was heat treated through a temperature cycle taking it above A^{of} first, holding for 1 hour and then cooling below M^{of} and warming back to room temperature. All strain gauges recovered their original state indicating full recovery of the specimen.

The results of this experiment can be used to extract the dynamic stress-strain response by applying the theory of one-dimensional wave propagation in plastic rods due to (Rakhmatulin, 1945; Von Karman and Duwez, 1950; Taylor, 1958). The idea is a simple extension of the rod theory for elastic waves. Let us assume that stress is only a function of strain, i.e. $\sigma = \sigma(\varepsilon)$. Then the balance of linear momentum (1) can be written in the form

$$u_{tt} = \frac{\sigma'(\varepsilon)}{\rho} u_{xx} \tag{55}$$

Note that this is not an incremental theory, but a total strain theory; therefore unloading cannot be considered here. The wave speed $C(\varepsilon)$ of disturbances is no longer a constant as in the linear elastic case, but a function of strain:

$$C(\varepsilon) = \sqrt{\frac{\sigma'(\varepsilon)}{\rho}} \tag{56}$$

The main result of this one dimensional theory is that a given strain (or stress) level will propagate into the rod with a characteristic speed given by equation (56). If the propagation speed of strain waves in a one-dimensional rod is known (measured with strain gauges as in the experiment discussed above), equation (56) can be inverted to determine the stress-strain behavior of the material:

$$\sigma(\varepsilon) = \int_0^{\varepsilon} \sigma'(\zeta) d\zeta = \rho \int_0^{\varepsilon} C^2(\zeta) d\zeta \tag{57}$$

This representation of the wave speed is used to extract the constitutive behavior of the material (Bell, 1960; Kolsky and Douch, 1962). There exists a critical point in the stress-strain curve: $\sigma'(\varepsilon) = 0$. Strain amplitudes larger than this cannot propagate through the material. Of course, in the experiment discussed above, we have not reached this stage; in fact, this would be of interest in determining the propagation of phase transformation fronts and such experiments are in progress.

The propagation speeds of different strain levels were obtained from the results shown in Figure 16. The time of arrival of different strain levels at each one of the five gauges were determined from the strain measurements. The speed of each strain level $C(\varepsilon)$ was then determined from the known distances between the gauges. The variation of the wave speed with strain level is shown in Figure 18; a smooth trendline is also shown in the figure. The elastic wave speed is about 2500 m/s and all strain levels below about 0.1% travel with this speed; this suggests that there is really no significant elastic region and that even small strain levels are susceptible to dispersion. A large change in the wave speed occurs at around 0.3% strain which corresponds to the

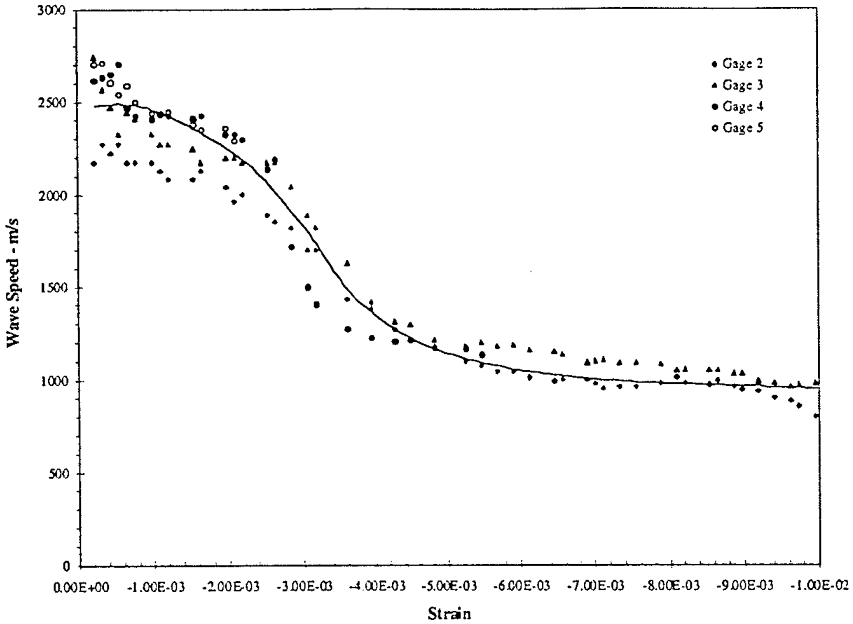

Fig. 18. Variation of the wave speed with the strain level as determined from the strain measurements. The line is an eyeball fit to indicate the data trend. Cubic fits over short segments were used to determine the wave speed corresponding to each strain level in the determination of the stress-strain behavior.

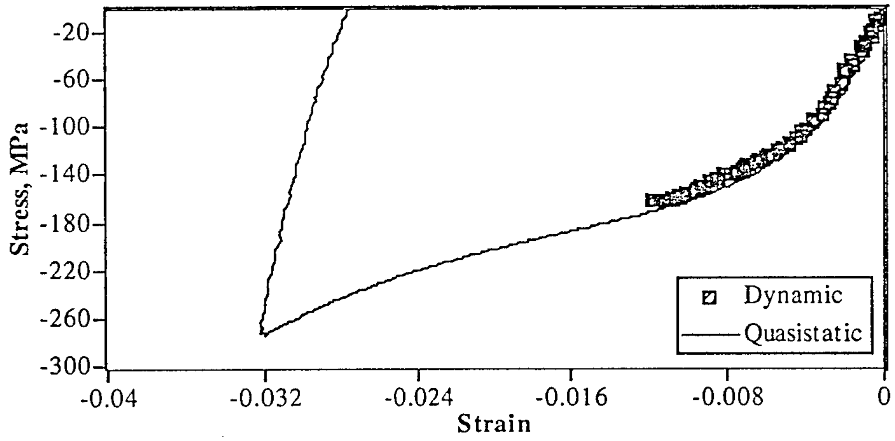

Fig. 19. Stress-strain response evaluated from one-dimensional wave propagation measurements (scatter plot) and quasi-static data (solid line).

onset of massive detwinning deformation. Beyond this level, the wave speed drops to about 1000 m/s and varies more slowly. If the averaged data on the wave speed variation with strain level is used in equation (57), the resulting numerical integration provides the stress strain relationship associated with the detwinning deformation in the SMA rod. Such a relationship is shown in Figure 19. The scatter in the plot is a result of the averaging of the noisy data in Figure 18; the solid line shows the trend of the data.

5.4 Numerical simulations of the Hopkinson bar experiment

A numerical simulation was performed and results were compared with the experimental data. As indicated earlier, due to a trigger failure, the signal in the input bar was lost so only the readings of the six strain gauges on the specimen were available. In order to supply proper boundary conditions the signal from the first strain gauge (at $10mm$) was used and the remaining gauges were simulated. Gauge number 3 was not included in the modelling because it unglued during the test.

The Hopkinson bar experiment was done at room temperature and due to the heat treatment of the specimen prior to the test it was in fully twinned martensitic state. The SMA model was applied in detwinning conditions (Section 2.3) with the material constants given in Table 3. The measured stress-strain response at room temperature and the simulated hysteresis are shown in Figure 15. The adaptive FEM scheme was chosen because of its accuracy and ability to predict precisely the positions of the both elastic and transformation shocks. The results are presented in Figure 20.

As expected from the numerical examples studied in section 4.1 the strain wave splits into an elastic and a transformation front. The transformation front timing and magnitude at all strain gauges is in good agreement with the experiment. The small oscillations observed at the first two gauges are due to surface effects caused by the impacting projectile. Such effects cannot possibly be modelled within a 1-D formulation.

There is, however, a noticeable disagreement in the timing of the elastic fronts. The reason for this is the deviations from linear behavior for small strains. The polynomial model always predicts a linear response until the beginning of the detwinning deformation. However an inspection of Figure 15 shows a smoother nonlinear stress-strain relationship for small strain values.

To verify the hypothesis that the disagreement is due to the initial elastic response of the model an independent numerical simulation of the dynamic experiment was performed. A phenomenological deformation plasticity model was used instead of the constitutive model of Section 2.3. The loading is assumed to have the form of a sixth degree polynomial that curve fits the loading part of the quasi-static hysteresis in Figure 15. The unloading was assumed linear, the slope being the modulus of martensite, $42GPa$, as measured by the quasi-static experiments. Due to the fact that the deformation is mostly detwinning of martensite there is no significant release of latent heat, so the quasi-static hysteresis is very close to the actual material behavior in the dynamic case (Figure 19).

The results of the simulation of the dynamic problem are shown in Figure 21.

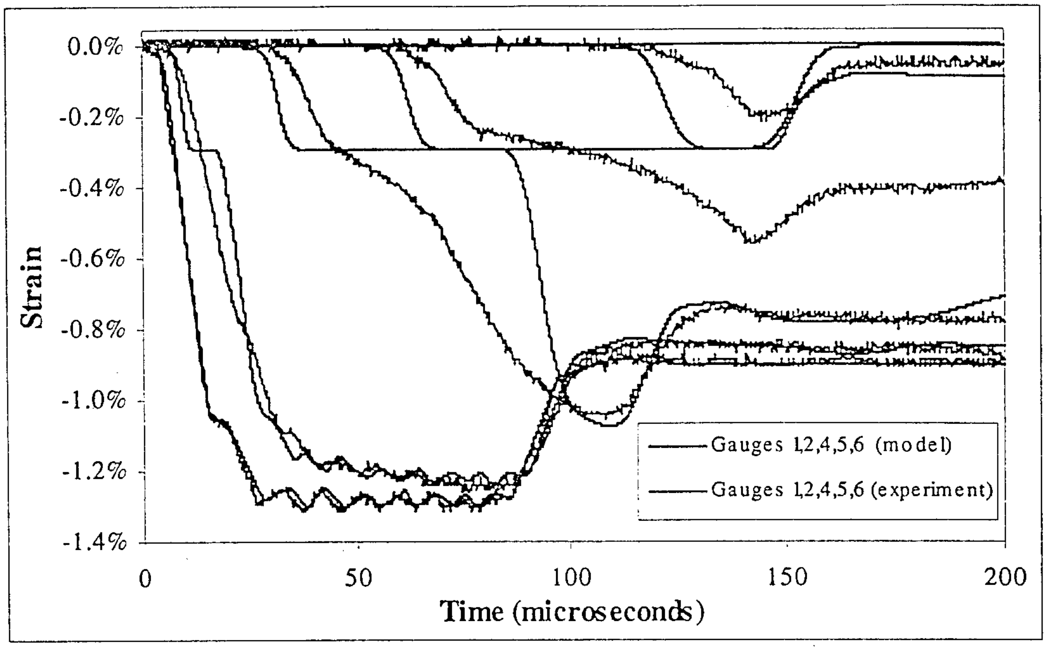

Fig. 20. And adaptive FE analysis of experimental data under isothermal conditions. The first strain gauge is used to define the boundary condition.

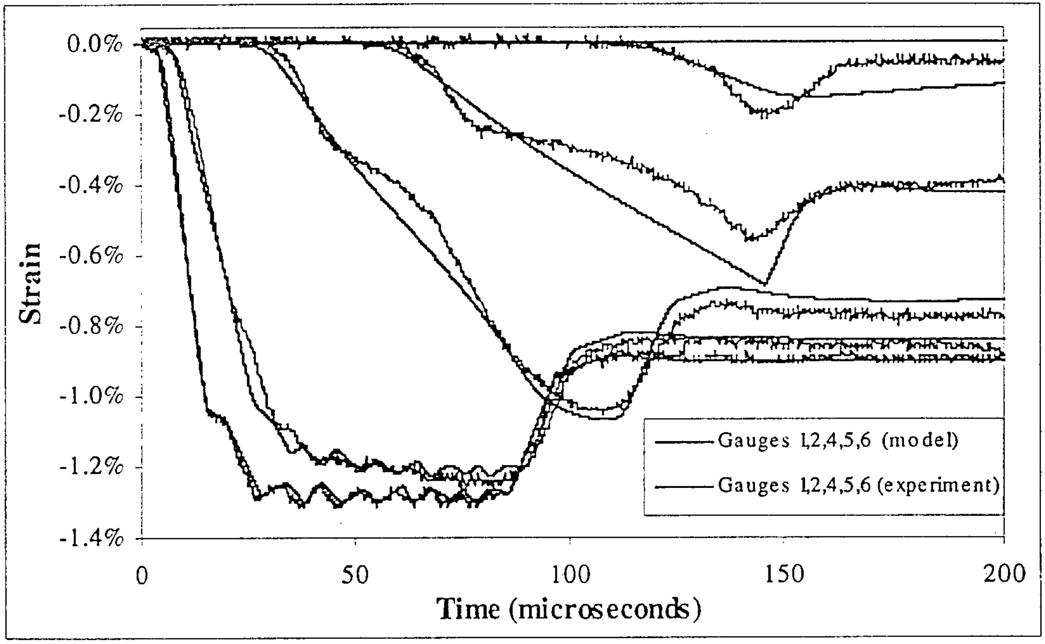

Fig. 21. And adaptive FE analysis of experimental data under isothermal conditions and a curvefit of the hysteresis. The first strain gauge is used to define the boundary condition.

This time the wave profiles are matched much more closely and the small disagreements can be attributed to measurement errors and effects of lateral inertia not included in the simulation. It should be noted that unlike a constitutive model based on physical principles such an approach will only work for a particular SMA specimen and particular operating temperature. However using a curve fit for the loading part of the hysteresis is sufficient to check whether disagreements between experiments and simulations are indeed due to the constitutive model.

6 Conclusions

The problem of dynamic loading of one-dimensional polycrystalline SMA rods has been explored numerically and experimentally. FEM simulations were performed for SMAs experiencing both pseudoelastic phase transformation as well as detwinning deformations. A long SMA rod was tested in a split Hopkinson bar experiment under detwinning conditions. The wave propagation was observed through strain gauges placed on the surface of the specimen. The strain history at the gauge locations obtained through numerical simulations of the dynamic experiment was found to be in good agreement with the actual results.

Computational solutions were shown to coincide with known analytical results. Nonlinear shock formation and velocities were captured correctly by the FEM simulations. The standard semi-discrete FEM approach for hyperbolic problems was complemented by an adaptive mesh refinement technique. The utilization of the Zienkiewicz-Zhu error indicator lead to an order of magnitude decrease of the computational time. Energy dissipation calculations for both detwinning of martensite and stress-induced phase transformation showed that the strain energy can be reduced by 80-90% which suggests that SMAs can be used effectively as shock-absorption devices.

On the experimental side, it has been shown that an instrumented Hopkinson bar can be used effectively to evaluate the wave and phase propagation characteristics in the SMA rods. Through the use of multiple strain gauges, the phase velocity at the different strain levels was obtained easily. An inelastic deformation theory was used to interpret the dispersion in terms of the underlying dynamic material response of the material. Dynamic and quasi-static material response were shown to be in excellent agreement.

Through careful calibration of the constitutive model for SMAs the peak strain levels of the Hopkinson bar experiment were accurately predicted. The main drawback of this model is its initial linear response in the case of detwinning and the existence of kinks in the hysteresis curve. Accurate predictions of the entire experimental data were obtained by using a polynomial curve fit of the quasi-static hysteresis of the material. Both the wave timings, shape and peaks were modelled within experimental error.

The material and environmental conditions used in the Hopkinson bar experiments correspond to a detwinning deformation of the martensitic phase, but the methods can be easily adapted to stress induced martensitic transformation in tests at higher temperatures. Theoretical work can also be extended to more realistic 2-D and 3-D geometries. Complicated SMA components and structures can be simulated to better understand the nonlinear wave propagation phenomena as well as the practical aspects of their energy dissipation capabilities. More refined models which incorporate both detwinning and pseudoelastic deformations simultaneously and also predict accurately the smooth hysteresis of the detwinning deformation will be extremely helpful in further studies of wave propagations in polycrystalline SMAs and are currently under consideration.

Acknowledgements

The authors would like to acknowledge the financial support of the Air Force Office of Scientific Research, Grant No. F49620-01-1-0196 monitored by Dr. Dan Segalman as well as the Office of Naval research Grant No. M00014-99-1-1069 monitored by Dr. Roshdy Barsoum.

References

Abeyaratne, R., Kim, S.-J., Knowles, J. K., 1993. One-dimensional continuum model for shape memory alloys. Int. J. Solids Struct. 41, 541–571.

Abeyaratne, R., Kim, S.-J., Knowles, J. K., 1994. Continuum Modeling of Shape Memory Alloys. New York, pp. 59–69.

Abeyaratne, R., Knowles, J. K., 1991. Kinetic relations and the propagation of phase boundaries in solids. Arch. Rational Mech. Anal. 114 (2), 119–154.

Abeyaratne, R., Knowles, J. K., 1993. Continuum model of a thermoelastic solid capable of undergoing phase transformation. J. Mech. Phys. Solids 41, 541–571.

Abeyaratne, R., Knowles, J. K., 1994a. Dynamics of propagating phase boundaries: adiabatic theory for thermoelastic solids. Physica D (79), 269–288.

Abeyaratne, R., Knowles, J. K., 1994b. Dynamics of propagating phase boundaries: Thermoelastic solids with heat conduction. Archive for Rational Mechanics and Analysis 126 (3), 203–230.

Abeyaratne, R., Knowles, J. K., 1997. Impact-induced phase transitions in thermoelastic solids. Phil. Trans. R. Soc. Lond. A (355), 843–867.

Bekker, A., Jimenez-Victory, J., Popov, P., Lagoudas, D., 2002. Impact induced propagation of phase transformation in a shape memory alloy rod. International Journal of Plasticity accepted for publication.

Bell, J., 1960. Propagation of large amplitude waves in annealed aluminum. Journal of Applied Physics 31, 227–282.

Bell, J., 1962. Experimental study of dynamic plasticity at elevated temperatures. Experimental Mechanics 2, 1–6.

Birman, V., 1996. Review of constitutive equations for shape memory alloys. In: Li, Y. K., Su, T. C. (Eds.), Proc. of 11th ASCE Conf. on Engineering Mechanics. Vol. 2. ASCE, New York, pp. 792–795.

Bo, Z., Lagoudas, D. C., 1999a. Thermomechanical modeling of polycrystalline SMAs under cyclic loading, part I: theoretical derivations. International Journal of Engineering Science 37, 1089–1140.

Bo, Z., Lagoudas, D. C., 1999b. Thermomechanical modeling of polycrystalline SMAs under cyclic loading, part I: theoretical derivations. International Journal of Engineering Science 37.

Bo, Z., Lagoudas, D. C., 1999c. Thermomechanical modeling of polycrystalline SMAs under cyclic loading, part III: evolution of plastic strains and two-way shape memory effect. International Journal of Engineering Science 37, 1175–1203.

Bo, Z., Lagoudas, D. C., 1999d. Thermomechanical modeling of polycrystalline SMAs under cyclic loading, part IV: modeling of minor hysteresis loops. International Journal of Engineering Science 37, 1205–1249.

Bodner, S., Clifton, J., 1967. An experimental investigation of elastic-plastic pulse propagation in aluminum rods. Journal of Applied Mechanics 34 (1), 91–99.

Boyd, J. G., Lagoudas, D. C., 1994. Thermomechanical response of shape memory composites. Journal of Intelligent Material Systems and Structures 5, 333–346.

Boyd, J. G., Lagoudas, D. C., 1996. A thermodynamic constitutive model for the shape memory materials. Part I. The monolithic shape memory alloys. Int. J. Plasticity 12 (6), 805–842.

Brinson, L. C., 1993. One-dimensional constitutive behavior of shape memory alloys: Thermomechanical derivation with non-constant material functions and redefined martensite internal variable. J. of Intell. Mater. Syst. and Struct. 4, 229–242.

Brinson, L. C., Lammering, R., 1993. Finite element analysis of the behavior of shape memory alloys and their applications. International Journal of Solids and Structures 30 (23), 3261–3280.

Chen, Y.-C., Lagoudas, D. C., 2000. Impact induced phase transformation in shape memory alloys. J. Mech. Phys. Solids 48 (2), 275–300.

Chiddister, J., Malvern, L., 1963. Compression-impact testing of aluminum at elevated temperatures. Experimental Mechanics 3 (81-90).

Clifton, R., Bodner, S., Jun. 1966. An analysis of longitudinal elastic-plastic pulse propagation. Transactions of the ASME 33, 248–255.

Cory, J.S., M.-J., 1985. Nonequilibrium thermostatics. J. Appl. Phys. 58, 3282–3294.

Escobar, J., Clifton, R., 1993. Pressure-shear impact induced phase transformation in cu-14.44al-4.19ni single crystals. J. Mater. Sci. Engng A (170), 125–142.

Feng, Z. C., Li, D. Z., July 1996. Dynamics of a mechanical system with a shape memory alloy bar. Journal of Intelligent Material Systems and Structures 7 (4), 399–410.

Fosdick, R., Ketema, Y., 1998. Shape memory alloys for passive vibration damping. Journal of Intelligent Systems and Structures 9, 854–870.

Funakubo, H., 1987. Shape Memory Alloys. Gordon and Bleach, New York.

Godlewsky, E., Raviart, P., 1996. Numerical Approximation of Hyperbolic Systems of Conservation Laws. Applied Mathematical Sciences. Springer-Verlag, New York.

Graesser, E. J., November 1995. Effect of intrinsic damping on vibration transmissibility of nickel-titanium shape memory alloy springs. Metallurgical and Materials Transactions A 26A, 2791–2796.

Graff, K., 1975. Wave Motion in Elastic Solids. Oxford University Press, London.

Jimenez-Vicktory, J. C., December 1999. Dynamic analysis of impact induced phase transformation in shape memory alloys using numerical techniques. Aerospace engineering, Texas A&M University.

Kolsky, H., 1949. An investigation of the mechanical properties of materials at very high rates of loading. Proc. R. Soc. Lond. B 62, 676–700.

Kolsky, H., 1963. Stress Waves in Solids. Dover Publications.

Kolsky, H., Douch, L., 1962. Experimental studies in plastic wave propagation. Journal of the Mechanics and Physics of Solids 10, 195–223.

Lagoudas, D., Bo, Z., Qidwai, M., 1996. A unified thermodynamic constitutive model for sma and finite element analysis of active metal matrix composites. Mechanics of Composite Structures 3, 153–179.

Lagoudas, D., Shu, S., 1999. Residual deformations of active structures with sma actuators. International Journal of Mechanical Sciences 41, 595–619.

Lagoudas, D. C., Khan, M. M., Mayes, J. J., 2001. Modelling of shape memory alloy springs for passive vibration isolation. In: Proceedings of IMECE01.

Liang, C., Rogers, C. A., 1990. One-dimensional thermomechanical constitutuve relations for shape memory materials. In: 31st AIAA/ASME/ASCE/AHS/ASC Structures, Structural Dynamics and Materials Conference. pp. 16–28.

Malvern, L., 1977. Introduction to the Mechanics of a Continuous Medium. Prentice-Hall Inc., Englewood Cliffs, N.J.

McNichols, J.L., C.-J., 1987. Thermodynamics of nitinol. J. Appl. Phys. 61, 972–984.

Nemat-Nasser, S., Isaacs, J., Starrett, J., 1991. Hopkinson techniques for dynamic recovery experiments. Proc. R. Soc. Lond. A 435, 371–391.

Newmark, N. M., 1959. A method of computation for structural dynamics. Journal of Engineering Mechanics Division, ASCE , 67–94.

Oberaigner, E., Tanaka, K., Fischer, F., 1996. Investigation of the damping behavior of a vibrating shape memory alloy rod using a micromechanical model. Smart Materials and Structures (3), 456–463.

Patoor, E., Eberhardt, A., Berveiller, M., 1996. Micromechanical modelling of superelasticity in shape memory alloys. Journal de Physique IV 6, C1–277–292.

Pence, T., 1986. On the emergence and propagation of a pahse boundary in ana elastic bar with a suddenly applied end load. J. Elasticity (16), 3–42.

Qidwai, M. A., Lagoudas, D. C., 2000a. Numerical implementation of a shape memory alloy thermomechanical constitutive model using return mapping algorithms. International Journal for Numerical Methods in Engineering 47, 1123–1168.

Qidwai, M. A., Lagoudas, D. C., 2000b. On thermomechanics and transformation surfaces of polycrystalline shape memory alloy materials. International Journal of Plasticity 16 (10-11), 1309–1343.

Rakhmatulin, K. A., 1945. Propagation of an unloading wave (in russian). Prikh.Mat. Mekh. 9, 91–100.

Reddy, J. N., 1993. An Introduction to the Finite Element Method. McGraw-Hill.

Siderey, N., Patoor, E., Berveiller, M., Eberhardt, A., 1999. Constitutive equations for polycrystalline thermoelastic shape memory alloys. part i. intragranular interactions and behavior of the grain. International Journal of Solids and Structures. 36, 4289–4315.

Sun, Q. P., Hwang, K. C., 1993a. Micromechanics modeling for the constitutive behavior of polycrystalline shape memory alloys — I. Derivation of general relations. J. Mech. Phys. Solids 41 (1), 1–17.

Sun, Q. P., Hwang, K. C., 1993b. Micromechanics modelling for the constitutive behavior of polycrystalline shape memory alloys — II. Study of the individual phenomena. J. Mech. Phys. Solids 41 (1), 19–33.

Tanaka, K., 1986. A thermomechanical sketch of shape memory effect: One-dimensional tensile behavior. Res Mechanica 18, 251–263.

Taylor, G., 1958. The plastic wave in a wire extended by an impact load, The Scientific Papers of G.I. Taylor,Vol.I,. Mechanics of Solids. University Press, Cambridge.

Thomson, P., Balas, G. J., Leo, P. H., March 1995. The use of shape memory alloys for passive structural damping. Smart Materials and Structures 4 (1), 36–41.

Von Karman, T., 1942. On the propagation of plastic deformation in solids. Tech. rep., NDRC Report No. A-29, OSRD No. 365.

Von Karman, T., Duwez, P., 1950. The propagation of plastic deformation in solids. Journal of Applied Physics 21, 987–994.

Wayman, C. M., 1983. Phase transformations, nondiffusive. In: Cahn, R. W., Haasen, P. (Eds.), Physical Metallurgy. North-Holland Physics Publishing, New York, pp. 1031–1075.

Yiu, Y. C., Regelbrugge, M. E., April 1995. Shape-memory alloy isolators for vibration suppression in space applications. 36th AIAA/ASME/ASCE/AHS/ASC Structures, Structural Dynamics, and Materials Conference , 3390–3398.

Zienkiewicz, O.C., Z.-J., 1987. A simple error estimator and an adaptive procedure for practical engineering analysis. International Journal for Numerical Methods in Engineering 24, 337–357.